A General Perspective of the Characterization and Quantification of Nanoparticles. Imaging, Spectroscopic and Separation Techniques

A. Lapresta-Fernández,[a*] *A. Salinas-Castillo,*[a] *S. Anderson de la Llana,*[b] *J.M. Costa-Fernández,*[c] *S. Domínguez-Meister,*[d] *R. Cecchini,*[e] *L.F. Capitán-Vallvey,*[a] *M.C. Moreno-Bondi,*[f] *M.-Pilar Marco,*[g] *J.C. Sánchez-López,*[d] *and I. S. Anderson*[h]

[a] ECsens, Department of Analytical Chemistry, Campus Fuentenueva, University of Granada, 18071 Granada, Spain

[b] Hôpitaux Universitaires de Genève, Service de Néonatologie et des Soins Intensifs Pédiatriques, Departement de l'Enfant et de l'Adolescent, rue Willy Donzé 6, Genève rue Micheli du Crest 22, Geneve, GE, CH 1205 Switzerland.

[c] Department of Physical and Analytical Chemistry, Faculty of Chemistry, University of Oviedo, 33006 Oviedo, Spain.

[d] Instituto de Ciencia de Materiales de Sevilla (CSIC – Univ. Sevilla), Avda. Américo Vespucio 49, CIC Cartuja, 41092-Sevilla, Spain

[e] Consiglio Nazionale delle Ricerche - Istituto per lo, Studio dei Materiali Nanostrutturati, (CNR-ISMN) - via P. Gobetti 101, 40129 Bologna, Italy

[f] Optochemical Sensors and Applied Photochemistry Group (GSOLFA), Department of Analytical Chemistry, Universidad Complutense, CEI-Moncloa, 28040 Madrid, Spain

[g] Nanobiotechnology for Diagnostics group (AMRg), IQAC-CSIC, CIBER de Bioingeniería, Biomateriales y Nanomedicina (CIBER-BBN), Jordi Girona 18-26, 08034 Barcelona, Spain

[h] Neutron Sciences Directorate. Oak Ridge National Laboratory. Building 8600, MS 6477, Oak Ridge, TN 37831, USA

***** Corresponding author: lapresta@ugr.es

ABSTRACT

This review gives an overview of the different techniques used to identify, characterize and quantify engineered nanoparticles (ENPs). The state-of-the-art of the field is summarized, the different characterization techniques have been grouped according to the information they can provide. In addition some selected applications are highlighted for each technique. The classification of the techniques has been carried out according to the main physical and chemical properties of the nanoparticles such as morphology, size, polydispersity characteristics, structural information and elemental composition. Microscopy techniques including optical, electron and X-ray microscopy and separation techniques with and without hyphenated detection systems are discussed. For each of these groups, a brief description of the techniques, the specific features and concepts, as well as several examples are described.

Table of contents

ACRONYMS AND ABBREVIATIONS 3
1. Introduction 5
2. Morphology, size and polydispersity characteristics 6
2.1. Microscopy techniques 6
2.1.1 Hydrated, liquid or gas samples by electron microscopy 12
2.1.2 Cryo-electron microscopy 16
2.1.3 Cryo-electron tomography 16
2.1.4 Scanning probe microscopy: AFM 17
2.1.5 X-ray microscopy (XRM) 18
2.2 Spectroscopic techniques 20
2.2.1. X-ray and neutron spectroscopy 24
2.3 Chromatography and related separation techniques. Size exclusion chromatography (SEC), capillary electrophoresis (CE), hydrodynamic chromatography (HDC) and field-flow fractionation (FFF). 25
2.4 Centrifugation, filtration and dialysis techniques. 30
3. Structural information and chemical composition. Single or hyphenated techniques 31
3.1 X-ray spectroscopy 32
3.1.1 Non hyphenated X-ray techniques 33
3.2 Other techniques coupled to EM 35
3.3 X-ray microscopy (XRM) 36
3.5. AFM and Brunauer-Emmett-Teller technique (BET) 38
3.6. Spectroscopic techniques for chemical identification 39
4. Elemental composition and concentration. 41
4.1 Mass spectrometry (MS) 41
4.2 Chromatography and related separation techniques 43
Acknowledgements 44

ACRONYMS AND ABBREVIATIONS

AFM	Atomic force microscopy
ADF	Annular dark-field
AE	Auger electron
AES	Auger electron spectroscopy
AgNPs	Silver nanoparticles
AUC	Analytical ultracentrifugation
AuNPs	Gold nanoparticles
BF	Bright field detector
BP	Breakdown probability
BSEs	Backscattered electrons
CE	Capillary electrophoresis
CEND	Coherent electron nanodiffraction
CFF	Cross flow filtration
CFM	Chemical force microscopy
CFUF	Cross flow ultrafiltration
CHA	Concentric hemispherical analyzer
CLSM	Confocal laser scanning microscopy
CMA	Cylindrical mirror analyzer
CNT	Carbon nanotube
CRM	Confocal Raman microscopy
CuNPs	Copper nanoparticles
CXDI	Coherent X-ray diffraction imaging
DLS	Dynamic light scattering
DF	Dark field detector
DIMs	Diffraction imaging microscopes
DMA	Differential mobility analysis
EDAX/ EDS/ EDX	Energy dispersive X-ray spectroscopy
EDXRF	Energy dispersive x-ray
EELS	Electron energy-loss spectroscopy
EFTEM	Energy-filtered TEM
EM	Electron microscopy
EPR	Electron paramagnetic resonance
ESEM	Environmental SEM
ESI	Electrospray ionization
ETEM	Environmental TEM
EXAFS	Extended X-ray Absorption Fine Structure
FCS	Fluorescence correlation spectroscopy
FE	Field emission
FFF	Field-flow fractionation
FIB-SEM	Focused ion beam SEM
FTIR	Fourier transform infrared spectroscopy
GISAXS	Grazing incidence SAXS
HAADF	High-angle ADF
HDC	Hydrodynamic chromatography
HPLC	High performance liquid chromatography
HRTEM	High-resolution transmission electron microscopy
ICP-MS	Inductively coupled plasma-mass spectrometry
LDI	Laser desorption/ionization
LIBD	Laser induced breakdown detection
LIBS	Laser induced breakdown spectroscopy
LIF	Laser-induced fluorescence
LSPR	Localized surface plasmon resonance
MALDI	Matrix assisted laser desorption/ionization
MALS or MALLS	Multi angle (laser) light scattering
MEMS	Micro-electromechanical systems
MoNPs	Molybdenum nanoparticles
MWCNT	Multi-walled carbon nanotubes

NEXAFS	Near-edge X-ray absorption fine structure
NMR	Nuclear magnetic resonance
NPs	Nanoparticles
NSOM	Near-field scanning optical microscopy
PCS	Photon correlation spectroscopy
PEELS	Parallel acquisition systems
PIMs	Projection imaging microscopes
POM	Polyoxometalates
PtNPs	Platinum nanoparticles
QDs	Quantum dots
RPLC	Reversed-phase liquid chromatography
SAED	Selected Area Electron Diffraction
SAM	Scanning Auger microscopy
SANS	Small-angle neutron scattering
SAXS	Small angle X-ray scattering
SEC	Size exclusion chromatography
SEM	Scanning electron microscopy
SERS	Surface-enhanced Raman scattering
SEs	Secondary electrons
SLS	Static light scattering
SPM	Scanning probe microscopy
SPR	Surface plasmon resonance
STEM	Scanning TEM
STM	Scanning tunnelling microscope
STXMs	Scanning transmission X-ray microscopes
SWCN	Single-walled carbon nanotubes
SXM	Scanning X-ray microscopes
TAD	Thin annular detector
TADBF	Thin annular detector used with bright-field
TADDF	Thin annular detector used with dark-field
TEM	Transmission electron microscopy
TPL	Two-photon luminescence
TOF	Time of flight
TSEM	SEM in transmission mode
TXMs	Transmission X-ray microscopes
WAXS	Wide angle X-ray scattering
WDS	Wavelength dispersive X-ray spectrometry
WDXRF	Wavelength dispersive Fluorescence X-ray spectrometry
XANES	Near-edge x-ray absorption spectra
XAS	X-ray absorption spectroscopy
XFEL	X-rays from upcoming free-electron lasers
XMCD	X-ray magnetic circular dichroism
XPS	X-ray photoelectron spectroscopy
XRD	X-ray diffraction
XRF	X-ray fluorescence
XRM	X-ray microscopy
XRR	X-ray reflectometry
Z	Atomic number

1. Introduction

Nowadays, engineered nanoparticles (ENPs) can be synthesized out of a large variety of different materials and possess a wide range of properties including size, shape, physical or chemical characteristics and elemental composition. Furthermore, interactions with the surrounding media can determine the colloidal stability of the particles, hence influencing their final state. Therefore, unexpected properties and interactions which are not solely dependent on elemental composition and state of aggregation,[1,2] but are more likely to be governed by surface area,[3] surface chemistry,[4] charge particle number,[2] size and size distribution,[5] aggregation,[6] structure[7] and shape[5,8] can lead to complex nano-systems whose properties differ from simple model theories.

This review deals with the use of different techniques, used either individually or in combination, to identify and characterize NPs depending on the desired property to be studied. Considering size distribution, degree of aggregation and morphology, imaging techniques based on different types of microscopies (optical, electronic, X-ray) and scattering (light, X-ray, neutron) techniques are described along with chromatography and related separation techniques. Elemental composition, structural information, and concentration are typically provided by spectroscopic techniques (*e.g.,* UV-vis absorption, luminescence and X-ray emission). Combining various characterization techniques (*e.g.,* electronic microscopy coupled with X-ray detectors) can provide information that cannot be obtained from each of the techniques individually. These so called hyphenated techniques can lead to a more complete characterization of NPs.

In the following sections a classification of different analytical techniques regarding the properties of the NPs, such as morphology, size, polydispersity characteristics, structural information and elemental composition is presented along with some related examples of application.

2. Morphology, size and polydispersity characteristics

As mentioned above, NPs show different properties depending on their morphology and size. Nowadays, the knowledge on materials composed of nanometer-sized entities is largely related to electron microscopy (EM) and scattering phenomena determining size and shape characteristics. Furthermore NPs separation has long been a key step in characterizing complex polydisperse nano/micromaterials. Although several analytical techniques can be used for these characterization purposes,[9] all available EM methods are limited by spatial resolution and/or the related detection limits.

2.1. Microscopy techniques

Since the nanoparticle is a nano-object with all three external dimensions in the nanoscale, the detection limit of optical microscopy does not often cover the NPs size since the visible wavelengths (λ) are comparable to the dimensions of the particles. To solve this limitation, a modified technique called near-field scanning optical microscopy (NSOM) can be used in its different configurations. NSOM is a scanning probe microscopy technique (SPM)[10] with a typical resolution between 50 and 100 nm, reaching 20 nm and 2-5 nm of lateral and vertical spatial resolution, respectively,[11] and even sub-20 nm for stripped gold pyramids.[12] It can be used to image aggregates of nanoparticles with a theoretical spatial resolution limited to λ/2 (see below). To detect fluorescent NPs, confocal laser scanning microscopy (CLSM) is applied with resolutions of the order of 200 nm[13] and it enables the visualization of the different accumulation of polymeric NPs in time at (sub)-cellular resolution in tumours.[14] Fluorescence imaging is restricted to intrinsically fluorescent NPs or fluorescently labelled NPs. The latter technique can introduce potential problems such as: label instability (leaching), modification of physicochemical properties or photobleaching.[15] Confocal Raman microscopy (CRM), which does not require labelling, allows, for example, the visualization of

toxicological effects of polymeric NPs in HepG2 cells and cellular NP uptake.[16] Moreover, by using the surface plasmon resonance (SPR) of metallic NPs (*e.g.,* gold nanorods) it is possible to image individual particle locations with optical microscopy by using Two-Photon Luminescence (TPL) and dark-field optical microscopes.[17] The latter technique provides a means of characterizing the size of gold NPs (AuNPs) by colour, since different colours such as violet, blue, green, and red are correlated with a size of 30, 50, 70, and 90 nm, respectively.[18]

Fluorescence correlation spectroscopy (FCS) uses confocal optics (a confocal microscope)[19] to evaluate diffusion coefficients of fluorescent NPs[20] or NPs with fluorescent coatings whose fluorescence fluctuations depend on the NP shape.[21] FCS allows to determinate size distributions in a very small laser illuminated volume (focal volume of approx. 10−15 μL) of very diluted solutions (10^{-8} to 10^{-15} mol·L^{-1}).

Electron microscopy (EM) techniques including transmission electron microscopy (TEM), and scanning electron microscopy (SEM); and scanning probe microscopies (atomic force microscopy (AFM)[22]) are particularly suitable for the characterization of NPs due to their intrinsic subnanometer scale resolution. These techniques are widely applied for NPs visualization.[19,23-25] EM techniques require vacuum conditions (~10^{-4} Pa) to allow both the operation of the electron source and to minimize scattering other than from the samples. The wavelength of electron beams depends on the acceleration voltage and is much shorter than the wavelength of light, hence allowing much higher spatial resolution down to single atoms in some cases. Thus, for an optical microscope operating at wavelengths, λ from 400 to 800 nm and numerical aperture (NA) of ~ 1, Abbe's diffraction limit d = λ/2NA, gives a resolution of approx. 200 nm[26] up to 10 nm with some improvement,[27] while for an EM working with an acceleration voltage from 100 to 1000 keV, the theoretical value of the wavelength will be from 0.0037 to 0.00087 nm[28] (See Table 1). Nevertheless, in the current

state-of-the-art, the best TEM resolution, by using double aberration correction, is 0.047 nm[29] while SEM microscopes achieve resolutions in the range of 1 nm (high resolution) to 3 nm (conventional).[28] In TEM, the electron beam (80-200 keV) passes through the sample and only NPs with a sufficient combination of electron density and size can be detected, being imprecise for cores smaller than 2 nm. At this point, high-resolution-TEM (HRTEM, 300 keV) reaches a 0.047 nm spatial resolution (see above), can image the crystallographic structure,[30] *e.g.,* edge length distributions or image 3D structures by combining different angular views, (the electron diffraction patterns can also provide structure information (see section 3)) and contributes to clarify the different behaviour of NPs from the bulk and free molecular state.[31] For biological materials, acceleration voltage is limited up to 100 keV, due to the damage caused in the sample by higher energy beams.

SEM produces images of the surface (or near surface) of a sample by scanning it with a focused beam of electrons (1 - 30 keV) and detecting the various signals that are produced when the electron beam interacts with electrons in the sample. The different signals that are detected (secondary electrons (SE), back-scattered electrons (BSE), characteristic X-rays, light (cathodeoluminescence (CL)), and transmitted electrons) provide complementary information concerning the near surface structure of the sample), though are rarely available all together. Accordingly, information of the surface topography is given by low energy secondary electrons (SEs), which are very sensitive to the sample charge and contamination. With high-energy backscattered electrons (BSEs), a mapping contrast based on differences in atomic number of elements as low as 0.1[28] is provided; consequently good contrast for heavy and light elements (*e.g.,* AgNPs in cells) is obtained.[32] Depending on the electron source used it is possible to change the spatial resolution, for instance, a low brightness tungsten electron source typically provides 50-100 nm resolution while brighter sources such as LaB_6 filaments allow a resolution below 5-10 nm. Using field emission guns (sharply-pointed Müller-type

emitter), the electron beam is more coherent reaching more intense beam of high energy than in conventional thermionic emitters such as tungsten and LaB_6 filaments. Table 1 shows the usual voltage range for SEM and TEM with the related relativistic and non-relativistic electron wavelength calculations.

Table 1

Conventional SEM can be operated in transmission mode (TSEM)[33,34] at low voltage (10 keV) for dimensional characterization of NPs with a minimum size of the order of 10 nm. Here, the detection of transmitted electrons can improve the signal-to-noise ratio, when comparing with detection modes that use only BSEs or SEs (the latter electron detection is less sensitive to the charge of the NPs.[35]

In a focused ion beam SEM (FIB-SEM), an ion beam substitutes for the incident electron beam and either secondary electrons or secondary ions, or both, can be detected and used for imaging. The technique is destructive in that it sputters the surface. Resolution is not as good as SEM, but using the milling and analysis technique it is possible to obtain a depth image in principle, 3D.[36] Focused charged particles (electrons, ions, and more recently clusters) can be used in scanning mode to reach sub-10 nm resolution allowing the observation of the milling process *in situ*. This technique is applied in a wide range of nanostructures for photonic purposes (*e.g.,* semiconductor NPs, carbon nanotubes (CNT)).[37]

Some common drawbacks are known when using TEM or SEM:

(i) they may be destructive techniques either due to sample preparation or beam damage.

(ii) Only allow the sample to be analyzed once (particularly in the case where the sample may be degraded by the beam, with the implication that it may be necessary to adjust beam energy (and hence resolution) to mitigate damage.

(iii) Since contrast is only good for materials with high electron density, biological samples are usually stained with osmium tetroxide in order to increase the contrast.

(iv) Both techniques work under vacuum conditions, so wet samples or those involving hydration artifacts, are not suitable.

(v) for conventional SEM imaging, samples must be electrically conductive, at least at the surface, or a conductive coating must be applied. Note that for FIB-SEM the sample surface can be neutralized with a separate electron beam hence obviating the need for a conductive surface.

To overcome these drawbacks, mainly staining and dehydration, additional techniques such as scanning TEM (STEM), environmental SEM (ESEM), environmental TEM (ETEM), both wet TEM and wet SEM and cryo-TEM (see below) have been developed.

In STEM, detailed sample information is obtained when a TEM electron beam is scanned over the sample. This information depends on the different range of generated electrons such as transmitted, secondary, back scattered, diffracted and emitted X-rays.[38] From all of them, higher signal levels and better spatial resolution are available when transmitted electrons are detected.[39] A wide range of voltages can be applied in this technique, low and intermediate voltages allow rapid throughput (0.2 nm resolution at 200 keV accelerating voltage, ideal for 1 nm and above). By applying high voltages (200–300 keV), better spatial resolution and analytical sensitivity are obtained. An image resolution better than 0.136 nm has been achieved with a nominal resolution of only 0.42 nm.[40] The expected resolution based on the fundamental equations that can be achieved by TEM, SEM and STEM, is presented by de Jonge et al.. [41]

STEM techniques can have multiple detectors operating simultaneously to collect different but complementary information. STEMs advantage is that it provides, either simultaneously or in a serial way, imaging, diffraction pattern and spectroscopic information.[38] Thus, STEM

can be coupled with a bright field detector (BF), showing the lattice images of NPs as in HRTEM. A dark field detector (DF) surrounds the transmitted beam to collect scattered electrons (diffracted beam) to create the image allowing to select different crystal structures to image. Similarly to dark-field imaging in HRTEM, it is possible to identify small particles in supported metal catalysts, defects in extended crystals and different phases in polycrystalline nanophase material.[38] Using BF and DF detectors toxicological studies of nanomaterials such as iron oxide NPs, single-walled carbon nanotubes (SWCNT) and cadmium selenide quantum dots (Cd/Se QDs)[42] have been undertaken. Electrons scattered outside the central beam in the diffraction pattern can be collected by an annular dark-field (ADF) detector placed in a circle around the electron beam (see figure 2). Increasing the inner collection angle of the ADF detector beyond the Bragg reflections in high-angle ADF (HAADF); in this case, only high-angle scattered electrons contribute to the collected signal, enhancing the atomic number (Z) contrast. DF offers high contrast without staining (usually with osmium tetroxide) with a sub-nm spatial resolution (<0.1 nm). Atomically resolved images have long been possible in STEM by using an ADF detector.[43] STEM paired with HAADF, is useful for imaging heavy elements such as silver or gold, (*e.g.,* AuNPs with 4 nm resolution[44] or smaller approx. 0.14 nm in a light-element matrix (e.g., organic tissue)[38] or Au nano-rods (1:6 width:length)[45] (resolution of 0.2 nm for non-corrected and 0.1 nm for aberration corrected instruments) operated at 200 keV). Currently, due to the introduction of aberration-corrected electron lenses at 300 keV, a spatial resolution of sub-50 pm (below 0.05 nm) is reached, allowing to determine the 3D structure of 10 nm AuNPs at a resolution of 0.24 nm.[46] Finally, a thin annular detector (TAD)[47] can be used with bright-field (TADBF), dark-field (TADDF) and also HAADF for both heavy and light-elements with atomic-scale resolution.[38] In case of analyzing NPs in bio-samples, a better resolution is achieved by STEM-BF than with ADF.[48]

With SE detection in STEM, subnanometer surface details of NPs can be revealed allowing to measure the work function of solid specimens and to study the charging effects of non-conducting materials.[38]

Auger electrons can be collected and analyzed by a cylindrical mirror analyzer (CMA) or a concentric hemispherical analyzer (CHA) electron spectrometer for surface compositional analysis (see section 2.2). Finally, further to the morphological characterization described in this section, it is possible to employ a spectroscopic analysis by the identification of single atoms analyzing their local electronic environment by coupling the EM with spectroscopic or nanodiffraction techniques (see section 3). Table 2 presents the EM techniques used for size distribution analysis and their related spatial resolution together with some examples of applicability, while Figure 2 shows a schematic representation of an EM, indicating the range of coupled analysis techniques that may be used.

Table 2

2.1.1 Hydrated, liquid or gas samples by electron microscopy

Where relevant, the particle characteristics should be measured under conditions that mimic their real environment. The challenge is to develop analytical techniques to detect and characterize properly NPs in complex matrices, such as aquatic media, while maintaining sufficient sensitivity to measure low concentrations of NPs. Several modified EM techniques are suitable to avoid artifacts brought about by sample dehydration, which allow the imaging of samples in liquid or under vacuum, at good resolution.[41] In almost all cases a dedicated sample holder, chip or chamber, made from silicon and hermetically sealed[49,50] is introduced in the system allowing atomic resolution in some cases and hence providing detailed information of NP growth models (see below). For liquid TEM, Liu et al., developed a

microchip holder made out of Si and epoxy resin of 1.3 x 1.3 mm and a 9 nm-thick SiO_2 observation window (150 x 150 μm^2). With a sample holder of path length of 2-5 μm allowing them to reach a resolution of 0.23 nm for imaging the (210) facet of tellurium NPs into living organisms in liquid samples.[51] Another type of wet cell has been developed by holding the fluid in a 200 μm frame sealed by two 50 nm silicon nitride windows, for imaging aluminium oxide (Al_2O_3) NPs and multi-walled carbon nanotubes (MWCNT).[52,53] Zheng et al., also developed liquid cells that allowed them to work in extreme conditions (at 120 kPa and temperatures up to 500 ºC) with TEM to visualize, at sub-nanometer resolution, the crystal growth of single platinum NPs (PtNPs) by coalescence or by addition of monomers.[54] In HRTEM, usual catalytic conditions (14 bar and 660°C) can be attained with micro-electromechanical (MEM) nanoreactors. Using such nanoreactors, structural changes in heated Pt dispersed on carbon black with a gas injection-specimen heating holder (300 °C in a vacuum of 5×10^{-4} Pa at 300 keV)[55] have been visualized. Similarly the atomic lattice fringes in Au[56] and CuNPs[57] have been imaged, down to 0.15 nm in the former case. Using a similar chip technology, it is also possible to use a microfluidic system for STEM measurements (wet-STEM). The chip is formed out of two custom designed silicon microchips, each supporting an optimal 50 nm thick window of silicon nitride connected to the outside of the microscope via plastic tubing. Resolution better than 0.2 nm for AuNPs[58] of 30 and 100 nm moving in liquid have been imaged with a 200 keV STEM. Similar approaches have been used to image NPs attached to the surface membrane of proteins of *E.Coli* and mammalian cells (COS7) in wet environments.[59] Currently, in wet-STEM with corrected spherical aberration (the electron beam is introduced into the liquid in a more localized and controlled way than in conventional TEM) it is possible to reach a resolution of 0.21 nm (lattice fringes for the (220) plane), visualizing the lead sulphide (PbS) NPs growing.[60] Note that bubble formation in the liquid cell can be avoided by optimizing the beam voltage by pulsed imaging.

Wet-STEM is suitable for imaging NPs (including NPs in gases above their saturated vapour pressure and liquid samples) under ADF imaging conditions. The technique can achieve resolutions of 5 nm (*e.g.,* for AuNPs) when using a field emission (FE) source; an improvement over standard measurments using SE and BSE detectors.[61] By decreasing the water layer thickness the wet STEM image contrast can be increased. Strong contrast is of special interest in polymeric NPs and biological samples, which otherwise give low contrasts because of their low atomic numbers.

ESEM and ETEM maintain a high vapour pressure around the sample, so working with fully hydrated or wet samples becomes possible (it is possible to dehydrate partially the samples by decreasing the vapour pressure in the chamber). In ESEM, the chamber containing the sample holder remains under a few mbar of gas as well as being saturated with water vapour.[28] Here, the vapour pressure can be decreased to achieve better NP imaging conditions (since only the surface of the water droplets are imaged at 100 % humidity, hiding the NPs that are inside them). The conductive coating over the sample in SEM is suppressed in ESEM, since the vapour gaseous layer around the NPs becomes ionized and neutralizes all charged regions (collisions of the electrons with the gas generate positive ions that prevent the build-up of charges on insulating samples). Furthermore, a signal amplification is produced by the generation of daughter electrons (cascade effect).[61] Thus, the resolution of ESEM can approach that of a standard SEM in vacuum, but as the liquid layer on the NP surface increases thickness the resolution drops dramatically.[41] A comparison between SEM and ESEM was carried out by Doucet et al.,[62] concluding that SEM provides sharper images and lower resolution limits (lower than 10 nm) but producing some dehydration artifacts (*e.g.,* aggregation). On the contrary, ESEM avoids these artifacts but image interpretation is more complex and the resolution obtained is lower (30-50 nm). ESEM also has been applied to soft nano-materials (*e.g.,* polymers) in the native state, overcoming the drawback of the

electrically insulating properties and radiation/vacuum-sensitive nature of such materials.[63] ESEM is also useful to visualize and to provide elemental analysis (see section 3) for cobalt (50–200 nm), nickel (50 nm), titanium (TiO_2 20–160 nm), silica (SiO_2 4–40 nm) and polyvinyl-chloride (PVC) (170 nm) NPs, in 10-μm thick tissue sections, placed over adhesive carbon discs inserted in the chamber).[64] Similarly, ETEM has been satisfactorily applied to study the catalytic activity (under O_2 or H_2 atmospheres) of Au and Pd NPs with the resolution of the (111) crystalline lattice plane[65] using an E-cell systems holder. Furthermore, ETEM permits visualization of NPs at high temperatures (1200 ºC or higher) and under gaseous atmospheric conditions (10 Pa or less) of the specimen chamber by using a temperature holder, hence enabling the analysis of the reaction processes in detail. For example PtNPs on Al_2O_3 have been imaged under conditions of 1 Pa O_2 at 1123 K).[66] The authors also made similar on graphite nanofiber (ribbon-type and platelet-type) with PtNPs under 10^{-3} Pa O_2 at 573 K. TEM studies make also possible elemental analyses using EDAX or EELS (see section 3).

An alternative to ESEM, is Wet-SEM [28]. This technique, seals the sample, for instance, in a steel holder developed by QuantomiX,[67] which uses a transparent electron membrane enabling the imaging of liquid samples (NPs in environmental matrices) by conventional SEM. Au (50 nm), TiO_2 (5 nm), ZnO (71 nm) and Fe_2O_3 (29 nm) NPs in distilled water, lake water and a soil suspension have been imaged by this technique.[6] The resolution obtained is between 10-100 nm.[13] Wet-SEM is a useful tool for *in situ* investigation of NPs and their aggregates in natural matrices and can be combined with an energy dispersive X-ray spectrometer to conduct qualitative/quantitative analysis (see section 3.1). Although all these techniques are promising and have been extensively used, it is still a challenge to focus on NPs in liquids due to the Brownian motion.[28]

2.1.2 Cryo-electron microscopy

To avoid dehydration artifact, NPs are kept frozen by cryo-TEM and cryo-SEM using a cryo-stage in the microscope under high vacuum. Thus, the glutaraldehyde for sample immobilization or chemical treatment (both involving sample alteration) are not necessary because of the physical fixation by freezing.[28] Cryo-TEM can reach a resolution of 0.2 nm imaging the gold plane (111).[68] In AgNPs, the lattice fringes spacing (0.207 nm) is also visualized in ionic liquid media (due to its low vapour pressure).[69] A resolution of 0.6-0.8 nm [70] can be reached when imaging AuNPs-protein arrays in 3D. Replacement reactions can also be visualized, *e.g.,* the electrostatic citrate shell is substituted by self-assembled polyoxometalates (POM) monolayers on the 5 nm AuNPs surface.[71] Working with cryo-SEM technique[72] (3-5 keV, -160 ºC, using SE and BSE imaging modes) it is possible to obtain a resolution from 1 to 3 nm[28] imaging the cellular internalization of polymeric NPs (250-300 nm).

2.1.3 Cryo-electron tomography

Cryo-electron tomography (cryo-ET) is an emerging structural technique which uses a combination of both cryo-TEM and tomographic methods. Here, the NPs are imaged by sections in three dimensions (3D) to an approximate 5 nm resolution.[73] This technique preserves samples at liquid-nitrogen temperatures, so the cells freeze without needing chemical fixing or additional staining.[74] Taveau et al., have used Cryo-ET to observe the nucleation and growth of polystyrene (PS) nodules on 170 nm silica seeds [75] being useful to visualize the growth of AgNPs by cathodic sputtering in ionic liquid.[69] Cryo-ET provides high resolution regarding information of pleiomorphic structures[76] or silica and AuNPs uptake by liposomes.[77] To observe the NPs in biological samples (frequently 80 keV or less), higher-than-normal microscope voltages (200–400 keV) are typically used to obtain higher specimen

penetration without losses in electron detection. The thickness for a 300 keV electron in organic materials is approximately 0.35 μm.[73] Several examples of NPs measured with different devices are shown in Figure 1.

FIGURE 1

2.1.4 Scanning probe microscopy: AFM

Atomic force microscopy (AFM), is a technique that belongs to the broader family of scanning probe microscopies (SPM).[78] In a cantilever (a very sharp probe tip) scans the sample and allows imaging of NPs (surface structure) in their natural environment with atomic resolution (approx. 0.5 nm for DNA height).[13] It is also possible to apply AFM to non-conductive samples in a wide range of media, including nanomaterials in liquid conditions (environments), hence overcoming the limitation of scanning tunneling microscopy (STM) in which only conducting samples can be imaged.[79] AFM resolution is limited by the size and geometry of the tip, which can be larger than the nanomaterial being studied and hence leading to an overestimation of the lateral dimension of the NP. There are several modes of AFM, (i) contact, (ii) non-contact[80] and (iii) tapping scanning or intermittent mode.[81] Contact mode (frequently used in static mode: without frequency modulation) is the most conventional imaging mode where the cantilever is deflected as it moves over the surface. The tip is constantly adjusted to maintain a constant deflection to "read" the sample topography. Due to the dragging motion of the tip, biomolecules or objects that are weakly attached to the substrate surface can be damaged or removed[82] and may eventually stick to the cantilever, hence leading to possibility of imaging artifacts. In an attempt to minimize those undesirable effects, (ii-iii) non-contact and tapping mode (typically with frequency modulation), where the tip only touches the surface momentarily, hence minimizing the physical contact, were

developed. In AFM different substrates are used such as mica, clean silicon (Si) and chemically treated silicon to deposit NPs. AFM allows the analysis of particles in their own environment[23] *e.g.,* natural aquatic colloids[83] in different types of water such as watershed (tapping mode),[84,85] drinking water,[24] or to image a size fractionation of natural aquatic NPs.[86] AFM is also successfully applied to the characterization of TiO_2, ZrO_2 and Al_2O_3 NPs,[87] semiconductor NPs such as CdSe/ZnS with 5–8 nm diameters and colloidal AuNPs with 15 nm diameter.[88] Furthermore, AFM has been used to study the effects of functionalized NiNPs on cancer cells[89] and the influence in the morphology of the cross-linker agent in thermoresponsive Au@NIPAM NPs.[90] AFM can also give chemical information about the sample (see section 3.5). Table 3 shows some of the properties related to the techniques used to characterize NPs in near native state by usual EM and AFM with some examples of applicability.

Table 3

2.1.5 X-ray microscopy (XRM)

Microscopy techniques based on X-ray photons can not only provide information on chemical composition and binding (See section 3) but also on structure and morphology. As with EM techniques, the spatial resolution achievable with a microscope is limited by the wavelength of the radiation and the optical elements used. We can classify two types of microscopes depending on whether focusing optical elements are used to focus the light by diffraction or not. The typical focusing element for X-ray wavelengths is a Fresnel zone plate. Microscopes that do not require focusing optics are classified as lensless projection imaging microscopes (PIMs) or diffraction imaging microscopes (DIMs).[91] As there are no lenses between the sample and the detector, higher resolution can be obtained, but it is limited by both the wavelength of the incident beam (synchrotron X-ray source) and by the strong decay of the

diffraction intensity.[92] In biological samples, these techniques also allow good resolution (11-13 nm) when labelling cells with AuNPs of 1.8 nm as used by Nelson et al..[93] 3D images can also be taken by high-contrast coherent X-ray diffraction patterns of Ag/Au nanoboxes (>100 nm) with spatial resolution of 4.2 nm[92] by Takahashi et al., while Newton et al., obtained 3D images of ZnO nanorods with 40 nm of spatial resolution.[94] By using coherent X-ray diffraction imaging (CXDI), where oversampled diffraction patterns can be inverted to obtain real space images, the facetted morphology of Pb nanocrystals[95] and single ZnO nanorods[96] have been imaged. Previously Isaacs et al., showed a diffraction pattern of a 160 nm silver cube.[97] Recently, the same research team, have been able to measure 400 nm diameter gold nanocrystal in higher resolution. The three-dimensional morphology and evolution of the strain under pressures up to 6.4 GPa were obtained with better than 30 nm spatial resolution.[98] Under low pressure, the edges of the nanocrystal became strained as expected, while under higher compression the strains disappeared, suggesting that the pressurised material is undergoing "plastic flow".

Two types of microscopes using optic elements are available: full-field transmission X-ray microscopes (TXMs) and scanning transmission X-ray microscopes (STXMs). TXM is mainly used for imaging while scanning X-ray microscopes (SXM) are used as an elemental analysis technique.[99] By the end of the 90´s, the structure of humic substances was visualized *in situ* for liquid samples reaching a resolution of 43 nm.[100] NPs preparation such as fixation, staining or sectioning are not necessary since the organic matter of some NPs (*e.g.,* iron oxides NPs) provides a much higher X-ray absorption than water. Although the TXM beam has higher energy than in STMX, causing more sample damage, it is more suitable than STMX for tomographic measurements since it takes faster images.[91] (STXM acquisition takes approximately 2 min per image). TXM is used for *in-situ* observation of the sulfidation process (hollowing effect) from Cu_2O crystals to Cu_2S cages into liquid phase for the first

time (photon energy range of 8–11 keV).[101] On the other hand STXM permits the analysis of structural changes due to aggregation effects in magnetite NPs (50 nm)[102] and the morphology of core-shell semiconducting polymer NPs (shell thickness around 10 nm and a core of 50–60 nm).[103] Quantitative compositional maps can be obtained by near-edge X-ray absorption spectra (XANES) (see section 3.1). Finally, 3D images with a resolution from 40 nm[104] up to 20 nm[105] are obtained by inversion of the coherent X-ray diffraction.

With lower photon energies (from ~250 eV (~5 nm wavelength) to 1.8 keV (~0.7 nm)), typically called soft-XRM, the X-rays reach a condenser zone plate giving a partially coherent hollow-cone illumination. This zone plate, in combination with a central stop and a pinhole, provides a monochromatic beam on a CCD camera. A spatial resolution below 15 nm is offered.[106] Soft-XRM in liquid media using a wet sample chamber (photon energy of 430 eV) gives a 40 nm resolution when imaging CdTe nanowires and hyperbranched PbS nanocrystals.[107] Extremely low energies (ca. 100 eV), used in Soft X-ray STXM, are useful for investigations of actinide dioxides of uranium (UO_2), neptunium (NpO_2) and plutonium (PuO_2). This technique also allows near-edge X-ray absorption fine structure (NEXAFS) for elemental mapping of actinide elements (see section 3.1) and imaging with 30 nm spatial resolution.[108] Finally, resolution at interatomic scale is possible by applying intense but brief pulses of X-rays from upcoming free-electron lasers (XFEL)[105] extending the X-ray microscopy to the femtosecond time domain. Nevertheless, FEL pulses are very bright and could involve sample destruction.

2.2 Spectroscopic techniques

The interaction between NPs and the electromagnetic radiation (electromagnetic waves, photons or electron beams) provides unequivocal characteristics. These characteristics involve composition information (See section 3), as well as NPs size and size distribution. Latter two

are presented in this section and can be studied by spectroscopy (mostly through scattering). Different sources of light such as laser, X-rays or neutrons can be used. By using a laser, light scattering helps determine particle size in a short time (minutes). The contrast in scattering light arises from the difference of the refractive index between the particle and water. To determine the size distribution profile and NPs aggregation in suspension, dynamic light scattering (DLS),[109] also called photon correlation spectroscopy (PCS) or quasi-elastic light scattering, is used. Fluctuations in the scattered light measured in DLS, can be originated from both (i) the Brownian motion and (ii) from the constructive or destructive interferences of the scattered light from the neighbouring particles. Although it is a rapid and simple method, this technique should be used in combination with another technique such as SEM or TEM[110] because of aggregates or dust, that can lead to underestimation or overestimation of results, involving a limitation in the interpretation, (especially for polydisperse systems).[111] Therefore, it is not possible to separate out the contributions coming from NPs of different sizes in the total population to the total correlation function. This is because the signal from larger particles dominates over that of smaller ones. Hence mathematical conversions to volume or number distributions from the intensity data, derived of DLS, can be erroneous and should only be properly provided with good knowledge of the particle shapes, polydispersity and underlying assumptions.[112] DLS is widely applied for the determination of average size, size distribution and polydispersity of *e.g.,* AgNPs,[113] AuNPs below 2 nm,[114] coated iron oxide NPs[115,116] or fluorescent polyacrylamide NPs.[117] Moreover, DLS measurements can be used to monitor the variation of the hydrodynamic diameter of the termoresponsive polymeric NPs (see figure 2).

FIGURE 2

Static light scattering (SLS), also called multi angle (laser) light scattering (MALS or MALLS), requires cleaner or sufficiently diluted samples compared to DLS. Here, the experimental variable is the time-average intensity of scattered light while in DLS it is the fluctuations in light intensity. SLS provides information on particle morphology for instance in suspension of triaxial cellulose nanocrystals isolated from cotton.[118]

Laser induced breakdown detection (LIBD) allows to detect both mean particle size and their concentration (See Section 3.6) in aqueous samples. Here, a laser beam with a fixed pulse is focused on the colloids reaching high temperature involving the dissociation of the material (breaks down) into excited ionic and atomic species. The analytical signal (the breakdown probability (BP)) can be related with the size of the NPs.[119] LIBD resolution is down to the 10 nm range.[120] In order to not saturate the breakdown probability, most samples have to be diluted, making it impossible to discriminate between different types of NPs. The most frequently used detection systems are CCD cameras (intensified (ICCD), non-intensified (CCD[121])) or piezoelectric crystals. As example, colloidal particles of hexavalent uranium (205-215 nm) can be determined.

Surface-enhanced Raman scattering (SERS) is a surface sensitive technique which measures the enhancement of Raman signals of Raman-active species due to the presence of NPs. Differences in the intensity of SERS signals reveal differences in morphologies and sizes (*e.g.,* between Ag nanospheres, nanorods and nanostars[122] or between Au nanoprisms showing a higher Raman enhancement than nanorods).[123] SERS was also applied to detect biocompatible and nontoxic PEGylated AuNPs for *in vivo* tumour targeting.[124] Noticeable is the contribution of the Liz-Marzán group in SERS field.[125-127]

UV-vis spectroscopy allows to determine not only composition information but also the NPs size and shape from the absorbance spectra.[128] The NPs size can be determined by studying the shape and position of the localized surface plasmon resonance (LSPR) peak.[129] Some

examples are now discussed. In the case of gold, the SPR for spherical AuNPs smaller than 2 nm is placed at 505 nm[130] while for 15-20 nm in size it is placed at 520 nm and for 100 nm it is around 575 nm. The longitudinal SPR mode for different Au nanorods aspect ratio (length: width) is placed from 650 to1000 nm. On nanorods the SPR band observed splits in two modes due to the different orientations of the rod in respect to the electric field of the incident light. Thus electron oscillation is produced across (transverse mode) and along (longitudinal mode) the long axis of the nanorod. The transverse SPR mode (at around 500 nm) only shows a minor shift when the Au nanorod aspect ratio varies. In contrast, the longitudinal SPR mode is significantly affected by the modification of the aspect ratio.[131] Similarly, spherical AgNPs present an absorbance band placed at 420 nm while Ag nanorods offer two bands placed at 420 and 615 nm.[122] Moreover, UV-vis has been used to detect biomolecular interactions taking place at the surface of the noble metal nanoparticles.[132] Thus, the SPR peak is also influenced by the refractive index at the adjacent surface interface of the nanoparticle, and this is affected by biofuncionalization or by binding interactions. An overview of functionalized gold nanorods used in a variety of analytical and biomedical applications is reviewed in details by Mannelli et al..[133]

UV-vis spectroscopy can be easily combined with different techniques such as chromatographic systems to enable size separation[134,135] or even with MALLS for the same purpose.[136] In combination with SEM, SAXS and XANES (see section 3), UV-vis spectroscopy has been applied to observe the size behaviour of AuNPs during different synthesis procedures.[137]

Finally, nuclear magnetic resonance (NMR) can be used for measuring the size of metal NPs encapsulated within dendrimers (differing in size by just a few tens of atoms)[138] as well as the size of colloidal matter.[13]

2.2.1. X-ray and neutron spectroscopy

Other sources of light such as neutrons and X-rays are used to determine sizes near (0.01–1 nm) and (1–1000 nm), respectively. Small or wide angle X-ray scattering (SAXS or WAXS) use flexible X-ray scattering to provide information of monodisperse samples about shape, size and structure. The size distribution is possible only in polydispersed samples via the form factor, *P*(q). SAXS does not show very good contrast between elements that are close in the periodic table since the contrast in X-ray scattering arises from the variation in electron density within the sample. In that case, it is possible to cause damage to the sample as a result of the large amount of energy applied (particularly at synchrotron sources). The NPs diameter and the size distribution are obtained from a scattering pattern. With near monodispersed particles, the scattering pattern of the X-ray shows concentric rings with a diameter directly related to the mean diameter of the NPs. SAXS has been employed to observe how the silica NPs interactions are decreased by the progressive dissolution of the tetrapropylammonium hydroxide functionalized surface (decreasing the surface charge when the NPs size decreases).[139] This technique is also useful to reveal core-shell structures, *e.g.,* in polymer coated iron oxide nanocrystals due to the high difference in electron density between the core and the polymer shell.[140] Suspensions of polymethyl methacrylate (PMMA) NPs with low polydispersity and diameters of 108 nm and 192 nm also have been imaged by SAXS.[141] X-ray reflectometry (XRR) combines small angle scattering with the reflection geometry to obtain dimensional properties of nanostructured surfaces. Here, by grazing incidence SAXS (GISAXS) structural parameters for 10 nm AuNPs[142] are determined. X-ray scattering coupled with UV-vis[128] allow to measure the mean size of AuNPs from the scattering data within 10% error.[143] SAXS also enables online analysis of the nucleation and growth of AuNPs avoiding uncertainties in the interpretation of UV-vis spectra.[137] This technique is also used to follow the growth of thiol-covered AuNPs at different reaction times.[144] Long

exposure times are used to obtain high-quality data sets (≈1 h) while shorter times predominate in case of high scattering intensity of the sample (*e.g.,* sizing distribution of AuNPs (reference materials)).[145]

By small-angle neutron scattering (SANS), the contrast arises from the different changes in the energy of the neutrons from different NPs (density and composition) and the magnetic moments of atoms involving a possible determination of both the chemical and the average spatial distributions of magnetic, *e.g.,* Fe_3O_4 NPs.[146] Moreover, it has been applied for the *in-situ* determination of the mean core diameter, the ligand length, and ligand solvation from dodecanothiol-AgNPs in gas expanded liquids.[147] Combining SANS and SAXS, it is possible to measure the size of carboxylic acid modified zirconia (ZrO_2) NPs in different solvents.[148] Table 4 displays some of the features related to the techniques used to characterize NPs depending on of size, structure and morphology among with some useful applications.

Table 4

2.3 Chromatography and related separation techniques. Size exclusion chromatography (SEC), capillary electrophoresis (CE), hydrodynamic chromatography (HDC) and field-flow fractionation (FFF).

NPs size characterization can be made by different separation techniques such as size exclusion chromatography (SEC), hydrodynamic chromatography (HDC), capillary electrophoresis (CE) and field-flow fractionation (FFF). All these techniques can be applied with other techniques or detection devices for further sample analysis.

SEC is a widely used technique for NPs isolation. The column is packed with porous packing materials, which form the flow channels. Particles which have a diameter smaller or equal than the pore size of the packing materials can permeate deep inside the column, while larger particles can only transfer through bigger pores or be excluded to extra-particular region. This

causes that smaller particles have longer retention times. Thus, SEC effectiveness for NPs isolation in water mainly depends on defining the pore size of the stationary phase to reject the particles with diameters that exceed the one specific for NPs.[149,150] It was successfully used for rapid determination of sizes and size distributions of AuNPs (from 10 to 80 nm[151] or from 5.3 to 38.3 nm[135,152]) and can be connected to a MALLS to obtain a molecular mass distributions.[153] Further development called recycling SEC allowed the high-resolution analysis (±0.6 nm) and size based separation of AuNPs having sizes below 3 nm.[154] Different shapes and AuNPs can be developed by SEC to examine the 3-D chromatograms obtained by employing a diode array detection system. These data are confirmed by TEM sizes.[155]

The separation of HDC particles[156,157] is based on their hydrodynamic radius.[158] The column is packed with microparticles that are nonporous, and the flow velocity and the velocity gradient across determine the separation.[159] Although the efficiency is very poor, the operating size range is very good. As the elution order is the same as in SEC and also in the steric mode of field flow fractionation (FFF), a further development of SEC consists in using HDC columns packed with non-porous beads and with a resolution between 5 to 1200 nm NPs size. This combination depends on the NPs flow velocity and the velocity gradient across them.[13,150] HDC has been combined with DLS for lipid nanocapsule separation[160] as well as in an interesting procedure using a silicon chip for channel separation using a CCD camera with a fluorescence microscope as detection system[161] or to detect species by UV absorption detection.[134] HDC coupled with ICP-MS is used to separate ‘‘real’’ environment samples by spiking AgNPs into sewage sludge. Initial data demonstrate that the AgNPs survive in the sludge supernatant, and could be successfully fractioned by HDC, even without filtration or centrifugation. TEM images also validate the results obtained by HDC-ICP-MS.[162]

Other types of chromatography as reversed-phase liquid chromatography (RPLC) are used to monitor the sizes of Au-Pt core-shell NPs.[163] Finally, high performance liquid chromatography (HPLC) is used in voltammetric detection for AuNPs separation.[164]

Species separation based on the charge and the size distribution is specifically allowed by CE. Recently, CE has emerged as one of the most potent separation techniques for inorganic ions, organic compounds, macromolecules and even biomolecules (*e.g.,* virus and bacteria). On the other hand, for selective separation of various NPs by size and surface-charge density (*e.g.,* latex particles, polystyrenes, inorganic oxide particles, metal particles and quantum dots) capillary-electromigration techniques are used.[165,166] Modifying some of the most important electrophoretic separation variables such as pH, buffer concentration, and organic modifiers, the rate of migration could be varied (*e.g.,* to separate AuNPs and Au/Ag core/shell NPs, evaluating also the average size).[167,168] A variation of CE called gel electrophoresis can be combined with other separation techniques such as liquid chromatography and coupled on-line to inductively coupled plasma-mass spectrometry (ICP-MS) to study the separation of AuNPs standards.[169] A review in the application of electrophoretic techniques for the separation of nanoparticles have been presented by Surugau et al.,[170] and a complete summary of AuNPs separation was attempt by Liu.[171] Latter provides an introduction to the characterizations of AuNPs using SEC, HPLC, electrophoresis, and their self-assembly onto solid supports for analyses.

FFF is a velocity based separation technique[172] that does not require a stationary phase for separation. Separation occurs by differential retention of NPs in a stream of liquid flowing through a thin channel when an external field is applied perpendicular to the channel.[173] The field drives components unequally into different streams according to the physical properties of the NPs, causing the separation from 1 nm until 100 μm.[111] In FFF, similarly to liquid chromatography, sample containing a mixture of nanoparticles is injected into a mobile phase

stream flowing through a thin, empty flow chamber, called 'separation channel'. The liquid flow drives the sample species along the channel. Unlike chromatographic techniques, FFF has no stationary phase. Actually, one of the key features of FFF is the absence of such a stationary phase. Therefore, undesired interactions of the nanoparticles with any stationary phase are avoided. Such, 'soft' fractionation mechanism result in a reduction of eventual sample degradations, aggregations or looses during the separation process. In FFF, separation is performed by the interaction of sample components with an externally generated field, which is applied perpendicularly to the direction of the mobile phase flow. The engineered nanoparticles present in the colloidal suspension (differing in size, chemical composition, surface functionalization and/or other physical properties) are carried downstream through the channel at different speeds, and exit the channel to the detector, at different retention times.[174] There are different operation modes of the FFF. In the Figure 3 it is schematized the "Normal operation mode". Here, retention times of nanoparticles are shorter for those with lower molar mass or size.

FIGURE 3

FFF can be used in/with different types of fields depending on the sufficient strength and selectivity to achieve the separation: centrifugal force (sedimentation FFF), gravitational (GrFFF), thermal (ThFFF), electrical (ElFFF), dielectrophoretic (DEP-FFF), Acoustic (AcFFF), magnetic (MgFFF) and hydrodynamic flow perpendicular to the separation flow (FlFFF). Latter can be found in two types: symmetric flow field-flow fractionation (FlFFF) and asymmetrical (AsFlFFF).[175]

FlFFF shows excellent size resolution and ability to investigate a wide range of sample and sizes, being promising for NPs fractionation.[176] FlFFF is based on hydrodynamic principles in which particles are separated due to their interaction with the cross-flow field force (friction coefficient) and their translational diffusion.[86] Further characterization can frequently be made

by on-line coupling detection devices as UV absorbance, DLS,[177] light scattering as MALLS to size separation of environmental colloids[178] or coupled with TEM (FlFFF–MALLS–TEM)[179] or AFM.[86] This technique can be applied for size characterization of diluted AuNPs using asymmetric flow FFF (AF^4).[180] AsFlFFF is useful for NP fractionation due to its high resolution and is applicable to a large size range. FFF can be coupled off-line with several analytical detectors.[150] Basically, to monitor the size distributions, the FFF needs to be coupled to a detector that responds to the nanoparticle number or mass concentration.

The measurement and characterization of nanoparticles (nanometrology) is critical in all aspects of nanotechnology, and particularly in environmental issues. Especially, in the field of environmental research, it has become clear that "complete" characterization of nanomaterials is critical for interpreting the environmental impact of the nanomaterials present in the environment.

Few analytical techniques can be successfully applied for NPs studies.[111] These methods each differ depending on the properties measured: average size, size distribution, surface characteristics, shape and chemical composition. Methods for assessing particle concentration and particle size distributions include electron microscopy, chromatography, centrifugation, laser-light scattering, ultrafiltration and spectroscopy.

Difficulties generally arise because of a lack of sensitivity for characterizing and quantifying particles at environmentally relevant concentrations (few micrograms per litre). Furthermore, the lack of specificity of the technique is problematic for complex environmental matrices that may contain natural NPs with polydisperse particle distributions, as well as heterogeneous compositions. In these conditions, FFF analysis, is a powerful tool for sizing and separating NPs. Particularly, coupling FFF with a sensitive and selective multielemental technique such as ICP-MS offers highly sensitive detection capabilities and provides direct information about nanoparticle composition.[181]

ICP-MS is a relatively straightforward elemental detection system to be coupled to FFF because the sample flow rate of the ICP-MS sample introduction system is similar to the outlet flow rate of the FFF system (0.5-2.0 $mL \cdot min^{-1}$). By using conventional detectors (*e.g.*, UV absorbance), the fractogram does not often differentiate between NPs of different composition and only shows the FFF separated particles by size. Nevertheless, the fractogram obtained using ICP-MS detection clearly shows the separated particles and the signal intensities for elemental composition of the NPs.[182]

Flow FFF techniques have been successfully utilized to characterize synthetic nanoparticles like carbon nanotubes,[183] or for the characterization of synthetic nanoparticles, such as CdSe/ZnS-MAA (mercaptoacetic acid) core/ shell-coated quantum dots (QDs).[184] Concentrations of manufactured nanoparticles in natural water in the range of 1–100 $\mu g\ L^{-1}$ have been estimated based on currently available data on nanoparticle production and guesses on potential releases into the environment.[185] Depending on their elemental composition FFF/ICPMS could be sensitive enough to be applied for their characterisation.

At present, one of the inherent limitations for quantitative applications of FFF-ICP-MS can be low recoveries, mainly due to undesirable physical interaction of the analytes with the membrane. Adsorption mechanisms result in nanoparticles sticking to the membrane that are not finally eluted. Different membrane compositions and mobile phases are investigated trying to minimize such a drawback of the technique.

2.4 Centrifugation, filtration and dialysis techniques.

Using these techniques, a particle size separation is obtained. Several parameters such as sedimentation velocity and sedimentation equilibrium experiments are observed.[13] To study suspended particles within the size range of small monoatomic ions, analytical ultracentrifugation (AUC) is a widely used. AUC has played a relevant role in nanoparticle

development due to the huge potential for macromolecular characterization.[186,187] Bootz et al., compared AUC with SEM, TEM and DLS techniques to determine the size and size distribution of the particle populations.[110]

Although filtration techniques allow particle size fractionation between 0.2 nm and 1μm[188] the fractionating size can be affected by both clogging and electrostatic interactions when using FFF.[189] Thus, for filtration and centrifugation, some artifacts may appear decreasing the effective pore size and can cause the retention of increasing amounts of colloids. This fact can be caused by the overloading of the membrane filters, in both microfiltration (pores size >0.1μm) and ultrafiltration (large sample volumes).[190]

NPs and ions can be also separated by using nanofiltration (pores of 0.5 or 1 nm). Since cross flow filtration (CFF) reduces the artifacts, it has become a standard method for the separation of colloids and particles. Cross flow ultrafiltration (CFUF) does not develop fully quantitative separation of colloids and particles in freshwater (1 nm- 1 μm). This fact was demonstrated by Doucet et al. comparing CFUF performance in the size fractionation of natural aquatic colloids against AFM and TEM.[85,191]

Dialysis is a very mild fractionation method and it can be used to separate truly dissolved components (ions and small molecules) from their nanoparticle counterparts.[111,192] Basically, these techniques (centrifugation and filtration) are mainly applied to sample preparation or in purification washing cycles.

3. Structural information and chemical composition. Single or hyphenated techniques

From the interaction between high-energy beams of charged particles (photons, electrons or X-rays) and the components of the NPs, unequivocal radiation related to each element can be emitted. Detection systems dealing with spectroscopy (absorption peaks, fluorescence or X-ray emissions), electron energy-loss or nanodiffraction techniques can be combined with

imaging techniques to give elemental and structural information. In the following sections, several individual or hyphenated techniques are discussed along with some applications to characterise NPs by these techniques.

3.1 X-ray spectroscopy

The generated X-rays from a sample are characteristic of each element or are related to the atomic structure. Therefore, the use of X-ray spectroscopic techniques enables us to detect subtle differences in atomic structure or chemical bond. These X-rays are obtained when an outer electron placed in a higher-energy shell is transferred to a lower energy level to fill the inner electron hole that has been excited by an incident electron beam. Energy dispersive X-ray spectroscopy (EDS, EDX, XEDS or EDAX,) identifies the atomic composition of the NPs by the generation of X-rays. EDX can be hyphenated to TEM or SEM to analyze the chemical composition of *e.g.,* dust NPs,[193] Pt@Fe_2O_3 core-shell NPs[194] or even to determine the possible antibacterial effect of silver ions.[195]

The combination of STEM and HAADF is suitable to identify structural variations of the AgPd@Pt NPs composition[196] or the concentration of gold in AuNPs using, interestingly, hair fibre as nanoreactor.[197]

In fully liquid conditions, it is also possible to develop elemental analysis by using liquid sample holders or microchips. EDS coupled with liquid-TEM helps confirming the growth of Pt nanocrystals by coalescence as an alternative to simple growth[54] and *the in situ* formation of tellurium NPs by microorganisms (see section 3.1.1.). In special conditions such as high temperatures and gaseous atmospheres, the visualization of PtNPs on Al_2O_3 is also possible.[66] Coupled with wet-SEM, the elemental identification of Au, TiO_2, ZnO and Fe_2O_3 NPs is reached.[6] Moreover, EDS coupled with ESEM has been used to monitor the biomedical

effects of several NPs such as metals (Ni, Co), ceramics (TiO_2 and SiO_2), and PVC[64] in rats muscles.[198] Figure 4 displays the EDX analysis of of Au/Ag alloy NPs imaged by TEM.

FIGURE 4

Wavelength dispersive X-ray spectrometry (WDS, also called WDXRF when using X-ray fluorescence) measures the X-rays coming from a specific and diffracted wavelength of the NPs. WDS is more precise than EDX and shows several improvements such as (i) a better energy resolution (ii) a peak-to-background capability to detect smaller amounts of elements[199] and (iii) a better detection of light atomic number (Z) elements. Combined with STEM,[200] the composition of Molybdenum NPs (MoNPs) can be given. As single technique, it is useful for the determination of Bismuth composition as residual synthesis component of magnetic metal oxide nanocrystals.[201] Furthermore, it is used to identify the residual Br^- and Cl^- capping agents on palladium nanowires in the catalysis of acetylene.[198]

3.1.1 Non hyphenated X-ray techniques

X-ray photoelectron spectroscopy (XPS) measures the kinetic energy of photoemitted (ejected) electrons when irradiating a sample with focused soft X-rays (typically below 1,5 keV).[202] As the X-ray photon energy is known, it is possible to determine the electron binding energy and identify the atomic core-level where the electron was extracted. XPS is useful to characterize NPs surfaces and coatings (*e.g.,* the evolution in the composition of Au/Cu NPs along the time in catalysis).[202] It is also used for the identification of encapsulated AuNPs into Cu_2S nanocages[101] and even for checking different chemical states of elements present in NPs (*e.g.,* the concentration of Au(I) in Au@Au(I) NPs and Ag in silica nanocomposites).[203,204]

In X-ray diffraction (XRD),[140] X-ray beams are projected over the NPs in a determined angle, called theta "θ", and the diffracted X-rays are collected in an angle of 2θ (See Table 5). XRD

allows structural phase identification of the NPs cristallinity (*e.g.,* between magnetite and maghemite NPs)[115,116] giving also the average particle size by using the Scherrer equation. Furthermore, different chemical states and elemental composition (*e.g.,* Ag into silica nanocomposites[204] or in nanocubes[205]) can be provided.

X-ray fluorescence (XRF)[206] results from the atom-localized emission when incident X-rays have higher energy than the ionization potential of the atoms in the NPs. Different types such as Wavelength X-ray separation (WDXRF) and energy dispersive X-ray (EDXRF)[13] can be used. Elemental composition of nanomaterials such as Ru-Pt bimetallic NPs[207] or ZnO nanoplates[208] is obtained.

(Table 5)

X-ray absorption spectroscopy (XAS) studies local atomic arrangements when intense and collimated X-ray beams (synchrotron radiation) reach the sample (See Figure 2). XAS can be divided in four energy regions: (i) pre-edge region < (ii) "rising edge" referred to XANES < (iii) NEXAFS < (iv) Extended X-ray Absorption Fine Structure (EXAFS) (corresponding to the scattering of the ejected photoelectron of neighbouring atoms). The combination of XANES and EXAFS is called XAFS. NEXAFS measurements allow further characterization of the organic material, identifying phenolic, carboxylic and carbonyl carbons. This specific characterization is possible due to the fact that each type of carbon is assigned to different eV peaks.[24] This improves the TEM-EDX analysis where all these analytes are grouped as only one carbon peak. XAS is used to detect small differences in the structure of colloidal nanocrystals[209] which can be difficult to discern using EM and XRD.[206] Nevertheless, structural evaluation of bimetallic NPs (Ru-Pt NPs)[207] is clarified by using EXAFS, XANES and XRD.[7] Moreover, it is possible to monitor different reaction steps[137] by checking both the

NPs surface passivation and the different oxidation states of CdSe quantum dots.[210] Moreover, latex particles are also imaged.[211]

Interestingly, using a photoemission electron microscopy, electronic and magnetic properties of single FeNPs (6-25 nm) can be measured with XAS and X-ray magnetic circular dichroism (XMCD) spectra.[212]

3.2 Other techniques coupled to EM

Electron energy-loss spectroscopy (EELS) is based on the energy analysis of the sample's inelastically scattered electrons (transmitted electron beam). EELS provides information on the electronic structure, surface properties, oxidation states and chemical composition at an atomic or subnanometer scale. EELS spectra are influenced by both the coordination chemistry (environment surrounding the atom) and the valence state of the atomic species (atomic core electron excitations). Parallel acquisition systems (PEELS) allow the simultaneous collection of data over a range of energy losses. Elemental analysis is possible for most elements, although in practice, the quantification is mostly applicable to the lighter elements with Z greater than 3. PEELS has superior detection efficiency for low Z elements compared with EDX (generally better suited for detecting elements of high Z). Both techniques show clear advantages for identifying and analysing higher Z components. EELS and EDX are complementary techniques and can be used to map composition in 2D or 3D.[213] Coupled with TEM or STEM they are successfully applied to elemental analysis (*e.g.,* of the oxide shell on the surface of FeNPs)[214] or to differentiate carbon nanotubes by metallic or semiconducting nature.[215] With the aim of increasing the energy-resolution in elemental analysis by SEM-EDX (usually limited between 100 and 150 eV and nearly two orders of magnitude larger than the energy resolution of EELS in TEMs/STEMs) a successful

combination between SEM and EELS is developed to acquire structural information with 4 eV of energy-resolution.[216]

EELS hyphenated to STEM[38] is useful to obtain maps of the SPR modes of single molecule SERS-active nanostructures.[217]

Energy-filtered TEM (EFTEM) forms images using only electrons coming from a particular energy-loss. EFTEM is useful for lighter elements[218] as well as to distinguish different materials in composites (*e.g.,* Nylon (22 eV)) from the nanotube (27 eV).[213]

Regarding nanodiffraction techniques, with STEM it is possible to obtain nanodiffraction patterns which provide nanostructure and morphology information from individual nanocomponents by coherent electron nanodiffraction (CEND). CEND is the only technique that gives full diffraction information about individual NPs, and is applied for instance to AgNPs smaller than 3 nm.[38]

Selected Area Electron Diffraction (SAED) paired with TEM or STEM gives information about crystalline properties of NPs,[23] *e.g.,* pattern of atomic Fe_3O_4 magnetic layer deposition on carbon nanocoils,[219] and allows to obtain atomic order information. Moreover, comparing with X-ray diffraction, bigger sample fields can be monitored.[150] All techniques described from sections 3.1 to 3.2 are shown in Table 6, among with several characteristics and applications.

3.3 X-ray microscopy (XRM)

XRM uses soft X-ray beams to image the samples, allowing both absorption and fluorescence signals to map the elemental and chemical composition of the NPs. XRM reaches a resolution between optical microscopy and EM in the so-called water window. Two types of microscopes are used in X-ray microscopy (i) full-field transmission X-ray microscopes for standalone and synchrotron sources (TXM and laboratory TXM (LTXM) where experiments

can be performed in the user's home lab) mainly used for imaging and particularly well suited for tomography, and the (ii) scanning X-ray microscope (STXM), mainly used for microanalysis and magnetization with high spatial resolution. In both techniques, Fresnel zone plates lenses for diffractive and spatially focused coherent X-rays are used. By TXM, it is possible to reach 3D images of Ag/Au nanoboxes (up 100 nm) not obtained by X-ray tomography with lenses nor atom probe microscopy or electron tomography.[92]

STXM can be used to monitor the presence of zinc in human cells exposed to ZnO NPs,[220] as well as to provide spatially resolved chemical state information of FeNPs[221] or to characterize actinide particles (100 to 1000 nm).[108] When combined with NEXAFS, the electronic and structural properties obtained by chemical mapping allow to distinguish core-shell structures in polymer NPs.[103] Different CNTs (from onion like or carbon NPs) and nanotubes synthesized by different growth methods[222] can also be distinguished. Notice that the analytical signal is 100-1000 times smaller for STXM than for techniques based on spectromicroscopy such as TEM-EELS, decreasing the radiation damage (See Table 6).[222] Figure 5 displays a schematic representation of electronic and X-ray microscopes.

FIGURE 5

3.4. Auger electron and Mössbauer spectroscopies.

A highly surface-sensitive technique such as Auger electron spectroscopy (AES) offers information about the surface topography and the surface composition of the NPs by collecting or analyzing Auger electrons (AE) emitted from the NPs surface (similar information is obtained with secondary electrons, SE). When an incident electron beam excites an inner electron, an outer electron can migrate to the created void in the inner shell. In consequence, energy is emitted, which is different to X-ray emission, and it is transferred

to a third electron on a further outer shell, leading to its ejection. AES was used to evaluate surface oxidative chemistry of AuNPs[3] and combined with SEM or STEM allows also chemical-composition analysis.[150] In STEM, sub-nanometer surface details can be observed at high-resolution SE images. AES can give qualitative and, in some cases, quantitative information about the surface composition of NPs consisting of multiple components.[38] For instance, it is applied to different types of chemical depositions such as diamond-like carbon on metal substrates (used as catalyst templates for the growth of CNTs)[223] and Prussian-blue analogues (PBA) NPs (from 6 to 25 nm) on silicon surfaces.[224] In Scanning Auger microscopy (SAM)[38] an image resolution <1 nm can be obtained which allows to detect as few as 15 silver atoms in AgNPs of a diameter smaller than 1 nm.[225]

Mössbauer spectroscopy is based on the resonant absorption and emission of gamma rays giving information about physical, chemical and magnetic properties of NPs. Gold-coated magnetic nanoparticles show the ability to yield high magnetic moments with the simplicity of bioconjugation on the gold surface. This type of NPs are suitable targets to be measured by Mössbauer spectroscopy,[226] which provides detailed information about magnetite NPs formation.[227]

3.5. AFM and Brunauer-Emmett-Teller technique (BET)

AFM allows to measure surface forces of the NPs for physicochemical characterization. AFM helps to identify chemical elements placed on the NPs surface by comparing with atomic force patterns[228,229] or by chemical force microscopy (CFM)[22] where functionalized probe tips are used.[230]

BET method is used for characterizing the porosity and surface area of solids, allowing the determination of the specific surface area by means of gas adsorption. For instance, it is

applied to measure the surface area of FeNPs[221] and the pore size distribution in SWCNTs[231] as well as to conduct toxicity studies.[232,233]

3.6. Spectroscopic techniques for chemical identification

LIBS belongs to the atomic emission spectroscopy techniques and consists in a short laser pulse irradiated on a sample creating highly energetic plasma that emits light at a specific wavelength peak according to the material. By identifying different peaks for the analyzed samples, their chemical composition can be rapidly determined. The number of plasmas (dielectric breakdowns) per number of total laser pulses and their spatial distribution in the laser focus can reveal both the colloidal concentration and size.[24] The LIBS plasmas depend strongly on the ambient conditions, the matrix effects and the signal to noise ratio.[234] LIBS reaches a low limit of detection (LOD) in the range of ppt ($ng \cdot L^{-1}$) allowing to analyze the NP size between 10 nm and 1 μm[235,236] as well as the particle number density (concentration) (see section 4) of colloids[237] and NPs (20 nm).[24]

By using double-pulse LIBS, some signals can be enhanced, such as for Al and Ca lines, up to five times compared to the single-pulse signal.[238]

Laser-induced fluorescence (LIF) and Raman spectroscopy allow the molecular structure characterization.[13] Electron paramagnetic resonance (EPR) detects unpaired electrons existing in a sample[239] and offers the possibility to analyze the particle surface reactivity. Due to the high sensitivity of EPR towards surface variations, it is possible to determine ligands in mixed monolayers which are covering AuNPs and also impurities on CdSe QD.[240] EPR is largely applied to NPs toxicity studies.[241]

UV-vis spectroscopy allows to obtain the NPs size and concentration (see section 4) depending on the position of the surface plasmon peak as Haiss et al., demonstrated for AuNPs.[242] Several chemical effects, that modify the optical behaviour of small metal

particles, can be studied by optical measurements focusing on the SPR displacement.[243] This displacement depends on both the surrounding environment of the NPs and the different types of surface functionalization.[244,245] Moreover, the particle concentration can be measured by using the molar extinction coefficient at the wavelength of the maximum absorption band (*e.g.,* in gold colloids).[246] Here, due to the difference in absorbance it is possible to determine Langmuir isotherms for the replacement of citrate by POM anions at the gold surface.[71] For AgNPs, the SPR shifts towards a longer wavelength as the solvent refractive index increases.[247] Depending on the composition of Ag/Au nanocages, different positions of the SPR of the metal nanocages[248] and hollow metal nanostructures[249] can be observed at the near-infrared region. Similarly, silver and gold can be used to form alloyed NPs which offer different SPR peaks at the visible range of wavelengths (See figure 6).

Finally, the effect of both humic acids attached to citrate-stabilized AuNPs and the pH can be observed by the reduction/displacement of the gold plasmon peak, leading to NPs agglomerations.[245]

FIGURE 6

Fourier transform infrared spectroscopy (FTIR) is useful to identify chemicals or to determine structural properties *e.g.,* in silver nanocomposites.[204] FTIR is used to identify the typical peaks for organic and inorganic NPs,[250,251] but often presenting an overlap between peaks that makes difficult to identify properly the different species or functional groups.[115] Changes in the absorbance bands of the NPs give details about composition. For instance, the presence of bovine serum albumin (BSA) shows a red shift of the AgNPs plasmon peak and the oxidation of AgNPs produces a broadening of the band width and a decrease in absorbance.[252]

SERS allows detecting single molecules by the enhancement of the Raman scattering signal (from a molecule) when it is located next to a nanostructured metal. Gold and silver nanoaggregates with attached reporter molecules can be identified by the Raman signature[32,253,254] as well as the ligand conformation on AuNPs.[255] In this field the contribution of Liz-Marzán et al. is of relevant interest.[256,257] All these techniques are displayed in Table 6.

Table 6

4. Elemental composition and concentration.

From a toxicological point of view, in addition to all the explained above characteristics, chemical composition is an essential issue to NPs identification. Specific techniques are related to characterize NPs, providing chemical composition of targeted NPs including if any, the core material and/or the surface layer composition. Moreover, several cases based on the NPs characterization by these techniques are also discussed.

4.1 Mass spectrometry (MS)

It is an analytical technique for element determination in which the sample is vaporized, ionized and measured by mass-to-charge ratio for quantitative purposes. Different ionization modes such as electrospray ionization (ESI) and laser desorption/ionization (LDI) can be used. ESI can be used *e.g.,* for the characterization of Au nanoclusters[258] while laser desorption/ionization of individual particles by soft ionization called matrix assisted laser desorption/ionization (MALDI) can be applied to detect products of ligand exchange reactions of the nanoparticles.[259] Inductively coupled plasma (ICP) uses high temperatures to dry, vaporize, atomize, and ionize the sample and generally is used for metal analysis. LDI can be applied to aerosol characterization by aerosol time-of-flight mass spectrometer (ATOF-MS),[13] providing valuable insights for functionalized NPs also by using time of flight

(TOF) as detection system.[260,261] The LOD of element gold can be as low as 1 part per trillion ($pg \cdot mL^{-1}$).[114]

ICP-MS can be coupled with separation techniques *e.g.,* with FlFFF for the elemental characterization of small colloidal materials[169] or with HPLC or electrophoresis techniques, not only for obtaining size fractioning NPs but also for determining chemical composition, relating distinct gel electrophoresis (GE) peak tailing with the chemical structure of the NP's surface.[169]

Different combinations with other techniques (SEM, TEM, AFM) and other analytical tools are possible (*e.g*., HDC- or FFF-ICP-MS, DLS).[162] On the basis of electrical mobility, using a differential mobility analysis (DMA), size differentiation and elemental composition are also possible.[13] Moreover, a detection system mainly composed by a laser induced fluorescence (LIF) and a quadrupole ion trap was useful to characterize fluorescence NPs by ion trap mass spectrometry of NPs.[262]

Inorganic mass spectrometry techniques may also offer great potential for the characterisation at the nanoscale, because they provide unique elemental information of great value for a better understanding of processes occurring at nanometre-length dimensions. Accordingly, several approaches for the characterisation (i.e. size, composition, presence of impurities, etc.) of colloidal solutions containing nanoparticles by the well-established ICP-MS technique can be found in the literature. The capabilities derived from the on-line coupling of separation techniques such as field-flow fractionation and liquid chromatography with ICP-MS allows a further exhaustive characterization of colloidal engineered nanoparticles.

In recent years, ICP-MS has become one of the most versatile and sensitive tool for elemental analysis in analytical chemistry[263,264] since most elements can be ionised in the ICP source. Routinely achievable until subnanogram per litre, detection limits have permitted the detection of ultratrace metal species in complex matrices. In addition, the dynamic range of

ICP-MS routinely exceeds 6 orders of magnitude, allowing detection of both major constituents and trace components at the same sample dilution. Therefore, quantification is rather easy and requires only standard solutions of inorganic elements. Furthermore, ICP-MS allows the straightforward use of isotopic-dilution techniques for most accurate measurements.

Recently, ICP-MS has been demonstrated to be a highly valuable tool for ultrasensitive detection and characterisation of metalloid-containing NPs and as a fast and reliable technique for quantification of NPs in solution. In this context, ICP-MS analysis of colloidal suspensions of QDs, with a core of CdSe and a shell of ZnS, was used to study the distribution of elements (Cd, Se, Zn and S) in both the core and the shell of the nanocrystals.[265] The accurate quantitative ICP-MS measurements (using isotopic-dilution inorganic mass spectrometry as a tool for characterisation at the nanoscale) of the NP colloidal suspensions were used to investigate the kinetics and to characterise the elemental composition of the core and shell with time.

Furthermore, ICP-MS coupled on-line to chromatographic and molecular fluorescence techniques can play a pivotal role in the assessment of CdSe/ZnS QDs synthesis, solubilisation and bioconjugation for their eventual use in reliable quantitative bioassays. Such a combination of analytical techniques allows the assessment of the effectiveness of the bioconjugations of QDs to antibodies, another important aspect rarely tackled so far.[266]

4.2 Chromatography and related separation techniques.

Although FFF is a specific size fractioning technique, thermal FFF can develop NPs identification. This is possible since one of the variables that affect the metal NPs retention is the particle composition being allowed to elute different NPs composition at different elution times (metal particles of Ag, Au ,Pd and Pt).[267] Moreover, FFF can be coupled to elemental

detectors as ICP-MS[185,268,269] for studying trace element speciation in natural waters.[270] A more complicated combination of techniques such as FlFFF-ICP-MS-TEM/X-EDS allows revealing the chemical composition of aquatic colloids and their interaction with trace elements as a function of colloidal size.[271] Tangential flow ultrafiltration method was efficiency used for size selecting and concentration of AgNPs minimizing the aggregation state.[272] In addition to concentration, speciation of the NPs can also be identified and quantified by FlFFF-ICP-MS.[185]

Collectively, it has become clear that the combination of different techniques that provide sizes and morphology information with more established techniques for elemental composition or structural identification can provide a full characterization of NPs. Nowadays, an extensive NPs knowledge is necessary *e.g.*, to minimize the environmental risks[273] associated to their size, morphology or composition.[239] However, depending on both the inner properties of the NPs and the environmental surroundings, the utility of these techniques have to be evaluated on a case-by-case basis. In each situation, preparing correctly the sample containing the NPs is a critical parameter that has special consideration.[274] As long as this critical step is successfully treated, the efficiency of the technique will be dramatically improved, obtaining more representative and more accurate information about the NPs in each studied conditions. Therefore, the approach towards a better understanding of the NPs behaviour and characteristics will allow a solid basis for the design of safer materials or materials with enhanced properties.

Acknowledgements

The work was funded in part by the Junta de Andalucía, (Spain) (Proyecto de Excelencia P10-FQM-5974) and CEI-Biotic Granada start-up Micro-projects for young researchers (CEI2013-MP-10). We would like to thank Dr. P. Buffat (EPFL, Switzerland) for his help.

Table 1. Usual range of voltages for SEM and TEM techniques with the associated electron wavelength. Relativistic and non relativistic calculations are considered. Therefore, these wavelengths correspond to the highest resolution that would be reached in each case.

	Accelerating voltages (keV)	Non-relativistic wavelength (nm)	Relativistic wavelength (nm)
SEM	0.5	0.05474	0.05473
	1.0	0.03871	0.03869
	10.0	0.01224	0.01218
	30.0	0.00707	0.00697
TEM	80.0	0.00433	0.00417
	100.0	0.00387	0.00369
	300.0	0.00223	0.00197
	1000.0	0.00122	0.00087

Table 2. Optical microscopy and electron microscopy (EM) to measure the size and morphological characteristics of NPs.

Optical microscopy						
Technique	Main Characteristic measured	phenomenon	Spatial resolution	Detector	comments	Applications in materials science
NSOM	Morphology; Size	Light-matter interaction	Lateral: sub-20 nm Vertical: 2-5 nm		Sub-20 nm resolution for stripped gold pyramids [12]	
CLSM	Fluorescence; Morphology; Size	Scattered, reflected laser light and any fluorescent emission	up to 200 nm[13]		Not always possible to distinguish between internalized NPs in the cells and NPs attached to the cell membrane, CRM better suited [16]	
FCS	Uses CLSM or Two photon excitation microscopy				Size distributions NPs [19]. NPs coating[21]	
Dried samples in Electron microscopy						
TEM	NPs visualization: aggregation, size, shape, dispersion, crystallographic structure	Electron beam passing through a thin layer of the specimen at high vacuum	Up to 0.07-0.05 nm		Biological samples acceleration voltage would be limited up to 200 keV. Dehydration artifacts	NPs morphology. Even core shells structure [115,116].
HRTEM			atomic distances		300 keV	CeO_2 NPs[30]
SEM	NPs visualization: surface topography, aggregation, dispersion, size and shape	Detection of scattered off electron when an electron beam is scanned over the sample at high vacuum	Up to 1-3 nm		Low energy electron beam (1 - 30 keV). SEs: surface topography BSEs: visible mapping contrast when the difference between Z of elements as low as Z= 0.1; dehydration artifacts	Metallic NPs in natural Environments [275]
TSEM		Detection of transmitted electron when a electron beam is scanned over the sample at high vacuum	~10 nm	BF and DF	Conventional TEM grids. ~30 keV	Silica, Au and latex NPs morphology [33,34]
FIB-SEM	3D sample imaging. Full imaging of individually collected sample sections		~ 10 nm		Fine focused beam of ions with a diameter down to ~5 nm	Nanostructured carbon materials [37]
STEM	Imaging, diffraction pattern or spectroscopic information NPs visualization: surface topography, aggregation, dispersion, size and shape. TEM electron beam scanned across the sample, transmitted, secondary, back scattered and diffracted electrons as well as the characteristic X-ray spectrum can be measured		~0.14 nm	BF	Higher atomic number: dark; No sample regions: bright	AuNPs (2.2 wt%) supported in mesoporous silica functionalized with a diethylenetriamine ligand [39]. Toxicity of iron oxide NPs, SWCNT and QDs [42]
			<0.1 nm	DF	BF detector includes the transmitted beam and so the holes appear bright whereas DF detector excludes the transmitted beam and holes appear dark	
			atomic	ADF	Energy, 300 keV; spherical aberration, 1.2 mm; illumination semi-angle, 7.98 mrad; defocus, 48.6 nm.	3D structure of 10 nm AuNPs at 2.4 Å resolution [46]
			0.14 nm	HAADF or Z-contrast	Information about structural variations across the sample on an atomic level. 200 keV. 3D electron tomography	Porous structure [276]; AuNPs and Au nanorods [45]; 3D-ET of CeO_2 NPs [30]
			atomic	TAD TADBF TADDF	Magnetic domains revealed	Heavy and light-element NPs [38]
			atomic	EELS	EELS is similar to X-ray absorption spectroscopy, but providing atomic-scale spatial resolution	Oxide shell characterization on Fe NPs[214]

[a] For abbreviations see text. Atomic distances: ~ 0.1 nm

Table 3. Analytical techniques to measure physical properties, structural information, elemental composition and concentration for some examples of NPs in near native state (liquid, gas).

Technique		Main characteristic measured	phenomenon	Spatial resolution	comments	Applications in materials science
Chip technology	Liquid TEM or wet-TEM	Size, shape, lattice image of NPs. Imaging in a wet environment or *in situ* liquid conditions by using a liquid cell (silicon made)	TEM beam passing through the thin window of a liquid cell sample holder	0.23 nm	200 keV. Combined with DF. Lattice-image of micro crystalline NPs	*in situ* imaging of TeNPs reduction by *K. pneumonia* [51]
					200 keV.	Al_2O_3 NPs, and CNT [52,53]
				Sub-nm	300 keV 100 nL o f sample	Pt nanocrystal growth [54]
	HRTEM	Silicon made MEMS-based nanoreactor that enables atomic-scale resolution at atmospheric pressure (GAS condition)		0.18 nm	300 keV. 100 kPa and up to 500 ◦C.	CuNPs formation in methanol production [57]
				0.15 nm	14 bar and 660°C	AuNPs [56]
	Wet-STEM	TEM electron beam scanned across a microfluidic system. NPs facet imaging		0.2 nm	200 keV, flow speed Q=2 or 5 $\mu L \cdot min^{-1}$.	COS7 labelled with AuNPs [58,59]
		Transmission observations of wet samples in an ESEM. Control of the sample surface in SE and BSE mode.		5 nm ; Combined with ADF	30 keV. Samples above their saturated vapour pressure.	AuNPs, silica NPs and grafted latex particles in water [61]
		NPs imaging in silicon chip.		0.8 nm ; 0.21 nm;	Combined with BF and DF. 200 keV, 15 ns electron pulses at 8 Hz.	Corrected spherical aberration PbSNPs [60]
ESEM		Morphology of hydrated samples maintaining a higher vapour pressure around the sample in the chamber		4 nm 10 keV	Resolution depends on the liquid thickness	Natural colloids [62] NPs of Co, Ni, TiO_2, SiO_2 and PVC [64]
ETEM		Size, morphology and structure lattice	Electron beam passing through the sample under different atmosphere conditions	0.17 nm 300 keV	Environmental sample holder designed for in situ chemical reaction studies	Au and Pd NPs behaviour in catalysis [65]. Al_2O_3 and graphite nanofiber with PtNPs [66]
Wet-SEM©		Fully liquid conditions to be imaged through an electron transparent membrane in a steel holder. Conventional SEM under hydrated conditions		5-100 nm	20–30 keV. Imaging elements with high atomic numbers; Metal in their environment	Au, TiO_2, ZnO and Fe_2O_3 NPs in distilled, water and soil suspension [6]
Cryo-TEM		Size, morphology, crystallinity, and aggregation NPs *in situ*	Electron beam passing through a frozen sample	0.207 nm	200-300 keV, (-175 to -190 [a]C)	AgNPs grown in ionic liquid[69]
				5 nm	120keV. Self-assembled POM on AuNPs [71]	
				Better than 0.2 nm	300 keV. -180 ºC. Imaging gold (200) planes of AuNPs[68]	
Cryo-SEM		Detecting the electrons scattered off the sample. Morphological data.		1-3 nm	5-10 keV, -130 ºC	Cellular uptake of polymeric NPs[277]
Cryo-ET		Imaging by sections of freeze samples.		5 nm	200 keV.Growth of PS and Ag NPs[69,75]; SiO_2 and AuNPs internalization[77]	
AFM		Surface imaging. Sharp probe in contact or not with the surface of the sample in their natural environment Si_3N_4 cantilevers with metal coatings (V-shaped).		Atomic resolution	1.5–2 volts with a scan speed of 1–2 Hz TiO_2, ZrO_2 and Al_2O_3, NPs[87]; CdSe/ZnS and AuNPs [88] Au@NIPAM NPs[90]. Natural aquatic colloids[24,83]	

[a] For abbreviations see text. Atomic distances: ~ 0.1 nm

Table 4. X-ray and spectroscopic techniques to characterize NPs in terms of size, size distribution, structure and morphology. Some selected examples are discussed.

Technique	Main characteristic measured	phenomenon	Spatial resolution	comments	Applications in materials science
X-Ray Microscopy					
XRM	X-rays pass through the sample towards a CCD detector. For hydrated samples, both phase and amplitude contrast are maximized when working in the "water window," the spectral region between the carbon and oxygen K-shell energies. [O (K: 543 eV) ~ C (K: 284 eV)] Large penetration depth of soft X-rays into the liquid media in comparison to electrons.		Better than 15 nm; spectral range from a photon energy of 250 eV (~5 nm λ) to 1.8 keV (~0.7 nm), so primary K and L atomic resonances of elements such as C, N, O, Al, Ti, Fe, Co and Ni can be probed[106]. Resolution: 40 nm in studies of the growth of CdTe nanowires and hyperbranched dried PbS nanocrystals [107].		
Soft- XRM					
TXM			Nanostructure evolution from Cu_2O crystals to Cu_2S cages in liquid phase, using a photon energy range of 8–11 keV [101]. Resolution: Cu_2S wall thickness of 10–20 nm.		
STXM	It focuses a highly monochromatic synchrotron X-ray beam by using Fresnel zone plates. Sample imaging by scanning the focal spot over the sample and measuring the transmission point by point		sub-10 nm	Structural changes in magnetite NPs (50 nm) due to aggregation at 1 keV [102] Core (50-60 nm)-shell (10 nm) polymer NPs [103]	
Soft X-ray STXM	It operates at ambient pressure removing influence of vacuum, uses fully sealed sample holders, requires a small amount of sample		Resolution around 500 nm for actinide dioxides of U, Np, and Pu [108]. Nevertheless, differences between the apparent size and the images are due to slightly different STXM focal settings		
CXDI	Scattering from the entire volume of the crystal at the Bragg reflection condition will interfere in the far-field, producing a three-dimensional (3D) diffraction pattern Measured (111) for Pb and (010) orientation for ZnO nanorods		40 nm	Growing Pb nanocrystals inside the vacuum chamber[95]	
			4.2 nm	Ag/Au nanoboxes [92]	
			40 nm	ZnO nanorods (7.2 keV corresponding to a wavelength of 1.72 Å) [94,96]	
			30 nm	400 nm diameter gold nanocrystal [98]	
			11-13 nm	750 eV photon energy. Labelling cell with 1.8 nm AuNPs [93]	
SAXS	X-ray scattering depending on the electron density of the NPs. It requires intense, monochromatic X-rays of low divergence.		Iron oxide core-polymer shell NPs [140]. 100-200 nm PMMA NPs using synchrotron radiation (photon energies from 6 to 10 keV) [141]		
GISAXS			AuNPs size (10-30 nm)[128,142]. Wavelength range below 1 nm corresponds to a photon energy of 1.24 keV, reaching 10 keV using monochromatized synchrotron radiation		
Spectroscopic Techniques					
DLS	Scattered light due to the interaction between the NPs and the source of light is related to the hydrodynamic NPs diameter		0.15 nm	Ag [113] AuNPs [114], polymeric NPs [278], Iron oxide (7-8 nm) silica coated NPs [115,116]	
SLS			5 nm	Cellulose nanocrystals [109]	
SANS	NPs scattered beam of neutrons as a function of scattering angle.		0.01 nm	Spatial distributions of magnetic moments of Fe_3O_4 NPs (9 nm).,magnetic shells 1.0 to 1.5 nm [146]. Dodecanothiol-AgNPs in-situ ligand solvation measurements[147] and ZrO_2 NPs [148] (SANS/SAXS).	
LIBD	Pulsed and focused laser excites the sample which atomically emits.		< 10 nm-1000 nm	Traces of hexavalent uranium (U(VI)) colloidal particles [119] *e.g.,* pulsed Nd:YAG laser and pulse repetition rate = 20-100 Hz	
UV-vis	Plasmon peak is related with the shape and size of the NPs		AuNPs of different shapes and sizes, including nanospheres, nanocubes, nanobranches, nanorods, and nanobipyramids [279]		
SERS	Inelastic scattering of photons from the incident laser light due to an electromagnetic and a chemical enhancement		SERS due to different shapes of Au or Ag NPs [122,123] Gold nanorods as SERS substrates for detection of scrambled prions [127]		
NMR	^{1}H NMR integral values of the innermost protons are modified by the NPs		^{1}H NMR experiment can be used to readily distinguish between dendrimers capsulated NPs [138]		

[a] For abbreviations see text. Atomic distances: ~ 0.1 nm

Table 5. Hyphenated techniques in electron microscopy and X-ray detectors. Information about structure and elemental composition of NPs (only selected examples are described)

Technique	Main characteristic measured	phenomenon	Combined	comments	Applications in materials science
X-Ray Spectroscopy					
EDS, EDX, XEDS or EDAX	High-energy beam of charged particles, such as electrons or protons or a beam of X-rays, is focused into the sample, registering the X-ray spectra. Elemental composition related to generated X-rays of an imaged NPs or their aggregates can be obtained		HRTEM	NPs composition [280]	
			FE-SEM UHV STEM	$Pt@Fe_2O_3$ core-shell NPs [194]	
			TEM	Antibacterial effects Ag(I) by interacting with thiol groups in proteins and inactivating the enzyme activity due the presence of sulphur [195]	
			ETEM	Liquid-Cell: PtNPs growth[54]. By Microchip-TEM TNPs[51]. Specimen holder allows high temperature and gaseous atmospheres, Pt over Al_2O_3 [66]	
			WetSEM	Au, TiO_2, ZnO and Fe_2O_3 NPs [6]	
			ESEM	Ni , Co, TiO_2,SiO_2, and PVC [64] in rat muscle	
			STEM	HAADF, morphology and composition of AgPd@Pt NPs in catalysis[196] and Au concentration in fluorescent AuNPs[197]	
WDS, WDXRF	Displays X-ray of a single wavelength at time without giving a broad spectrum of wavelengths or energies simultaneously as EDX.		STEM	MoNPs (25keV) [200]	
			SP	Bi composition as residual synthesis component of magnetic metal oxide nanocrystals [201]. residual Br^- and Cl^- capping agents on Pd nanowires[198]	
XPS	Kinetic energy of photoemitted electrons when irradiated a sample with focused X-rays with photon energy range of 8–11 keV Synchrotron [101]		SP	Au-CuNPs evolution [202]. Confirmation of Au(I) on Au@Au(I) [203]., chemical states of Ag into silica nanocomposites [204] Cu_2S nanocage composition with encapsulated AuNPs [101]	
XRD	Impinging X-rays over the sample satisfies the Bragg's equation, constructive interference occurs, sample rotates in the path of the collimated X-ray beam at an angle θ while the detector rotates 2θ		SP	Magnetite [115] and maghemite [116] core composition into fluorescence silica shell NPs Ag nanocubes patterns [205], Iron oxides composition encapsulated in polymer [140]	
XRF	Short X-ray or gamma -ray with energy higher than the ionization potential of atoms in the sample induces emission of characteristic fluorescence.		SP	Composition of Ru-Pt bimetallic NPs [207] or purity of ZnO nanoplates [208]	
XAS	Incident photon interacts with the electrons bound in an atom. The energy of the incident photons is sufficient to cause excitation of a core electron of the absorbing atom to a continuum state to produce a photoelectron. 1s: k-edge; 2s, 2p:L-edge; 3s,3p,3d: M-edge		Synchrotron	Pre-edge; XANES; NEXAFS; EXAFS. Latex particles and microballoons dispersed in water [211]. Structural determination of Ru-Pt NPs [207], QD surface passivation [210]	
Others techniques coupled to EM, elemental information					
EELS	Measure of the energy-loss of incident electron when passing through the sample		TEM	Electronic structure of the oxide shell on the surface of FNPs [214]. Differences in metallic or semiconducting CNTs [215]	
			SEM	Carbon film at 30 keV beam energy [216]	
			STEM	Image SERS hot spot [217]	
			EFTEM	Discrimination in a composite the different plasmon excitation energies of the nylon (~22 eV) and the nanotube (~27 eV)	
CEND	Diffraction information about structure and morphology		STEM	<3 nm in diameter AgNPs [38]	
SAED	Diffraction patterns of the impinging electrons due to the atoms of the sample act as a diffraction grating		TEM	Atomic layer deposition is applied to coat carbon nanocoils with magnetic Fe_3O_4 or Ni [219], SAED pattern of Ag nanocubes patterns [205]	

[a] For abbreviations see text. Atomic distances: ~ 0.1 nm. SP: Spectrometer

Table 6. X-ray microscopy, spectroscopic techniques and Auger, Mössbauer and BET techniques. The most important issues related to some NPs applications are described for each technique

Technique	Main characteristic measured	phenomenon	Applications in materials science
X-RAY Microscopy			
STXM	Use radiation in the energy range 250 to 3000 eV, focused by Fresnel Lens, being then the sample scanned perpendicular to the optical axis, while the intensity of the transmitted X-rays is detected at the same time.		ZnO NPs in cells [220], down to ~20 nm in carbon nanotubes [222], Polymer NPs compositional maps [103]. Chemical state information of Fe and actinide NPs (100 to 1,000 nm)[108].
TXM			3D electron density mapping of Au/Ag nanoboxes ~ 100 nm [92]
Other techniques			
AES	Surface-sensitive technique related to the inelastic scattering that occurs for electrons; Most of the emitted Auger electrons are produced within a very short distance from the sample surface, typically 0.3–3 nm.		Catalyst layers and the CNT systems [223] Prussian-blue analogues (PBA) NPs (from 6 to 25 nm) over silicon surfaces [224].
Mössbauer spectroscopy	Resonant absorption and emission of gamma rays for energy level transitions gives information about the atom's local environment		Fe_3O_4 NPs pathway formation [227]
BET	Physical adsorption of gas molecules on a solid surface.		Specific surface area and pore size distribution of SWCNTs [231] and on FNPs (gas adsorption 3 $m^2 \cdot g^{-1}$ with a diameter (Φ) between 38-45 nm) [221]
Spectroscopic techniques to determine NPs concentration			
LIBS	The strong heating of the sample leads to a ionized light (plasma) related to the chemical elements		Quantification of particle number density [24].
LIF	Excited NPs by a laser and the fluorescence spectrum is analyzed		Structural species characterization [13]
EPR	Detection of unpaired electron in or related to NPs.		Impurities on CdSe QDs[240] Induced OH^- species by iron oxide NPs [241]
UV-vis spectroscopy	Position of the UV-vis peaks are related with size, shape and NPs composition		Ag/Au nanocages composition [248] Hollow metal nanostructures [281]
FTIR	Chemical bonds in a molecule results in absorption peaks		Structural properties of e.g., Ag nanocomposites [204]. Iron oxide core-shell silica NPs[115]
SERS	Enhancement of a Raman intensity peak through changing the composition and the morphology of the NPs		Ligand conformation on AuNPs [255] Au nanostructures modified with silver [256]

[a] For abbreviations see text. Atomic distances: ~ 0.1 nm

FIGURE LEGENDS

Figure 1. (a) and (b) cryo-TEM of silica NPs. (b) It shows an self-assembly of nanoparticles in higher-order and defined structures in 2D. (c) TEM of magnetite (Fe_3O_4) NPs. (d) Cryo-TEM of core-shell NPs (magnetic core@silica shells). (e) TEM of Carbon Dots. (f) FIB-SEM of Au NPs where it can be seen the laser size effect, involving an important limitation to observe the interior of the NPs. (g) TSEM of hybrid NPs (gold@polymer), (h) TEM image of gold NPs (Φ =30 nm) (i) HRTEM of seed and grown AuNPs (Φ =100 nm). (j) and (k) are TEM of Au nanorods and branched morphologies.

Figure 2. TSEM of polymeric termoresponsive NPs (a) and (b) TEM image of a dilution of NPs imaged by the picture "a". (c) Variation of the hydrodynamic diameter of stimuli-responsive polymeric NPs, with temperature. Closed and open symbols denote the cooling and the heating cycles, respectively. Continuous (Cooling) and dashed (Heating) lines correspond to the Boltzmann fit of the experimental values. The inset is a typical view of the size distribution of the NPs by DLS.

Figure 3. Normal operation mode in FFF. (Reprinted from publication ref. 174, Copyright (2005), with permission from Elsevier.)

Figure 4. Information obtained by a EDX coupled to a TEM. (a)TEM image for alloy Au/Ag 15:85 ratio NPs, (b) corresponding EDX spectrum. Peak at (8.04 keV) are from the copper of the support grid.

Figure 5. Schematic diagram of electron microscopy (EM) and scanning transmission X-ray microscopes (STXM) together with generated signals for high-resolution images, nanodiffraction patterns or spectroscopic related to NPs characteristics. Transmission electron microscopy (TEM), scanning electron microscopy (SEM), focused ion beam SEM (FIB-SEM), scanning transmission electron microscopy (STEM), energy dispersive X-ray spectroscopy (EDX), Auger electron spectroscopy (AES) and scanning Auger microscopy (SAM), secondary electron microscopy (SEM), wavelength dispersive X-ray spectrometry (WDS) electron energy-loss spectroscopy (EELS), coherent electron nano-diffraction (CEND) and selected area electron diffraction (SAED). Bright field (BF) and large angle BF (LABF), dark-field (DF), annular dark-field (ADF) and high-angle annular dark-field (HAADF); Into STXM: Lensless projection imaging microscopes (PIMs) or diffraction imaging microscopes (DIMs)

Figure 6. TEM images of (a) AgNPs (size around 40-60 nm), (b) AuNPs (size around 20-30 nm) (c) . Uv-Vis- spectra of AgNPs (416 nm), AuNPs (521 nm) and alloys NPs made of different Au:Ag ratios, being 15, 25 and 50% content of Au placed at 426, 442 and 463 nm, respectively (sizes 40-60 nm). (d) Observed visual range for Au/ Ag alloy NPs.

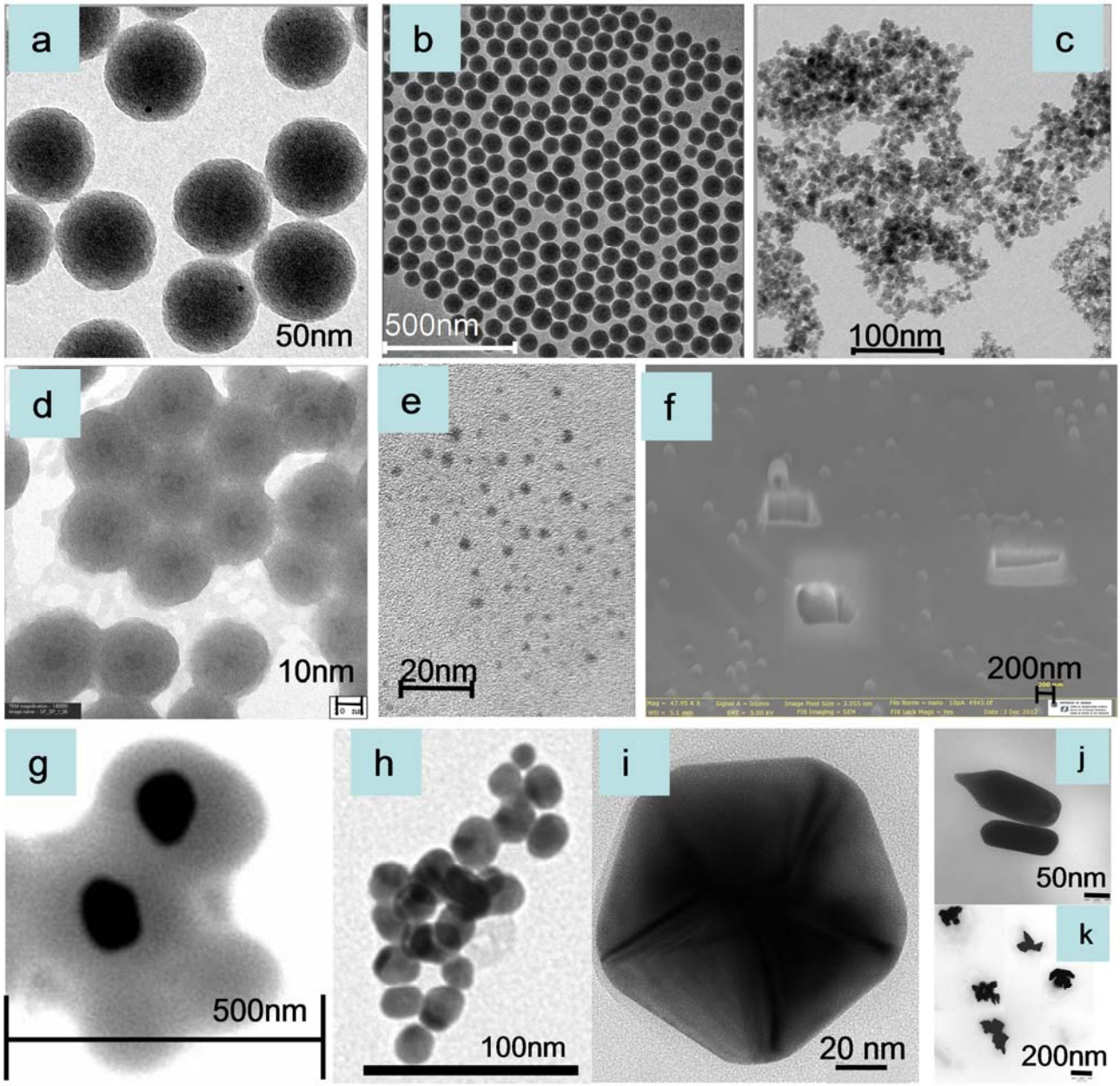
a
50nm
b
500nm
c
100nm
d
10nm
e
20nm
f
200nm
g
500nm
h
100nm
i
20 nm
j
50nm
k
200nm

Figure 1

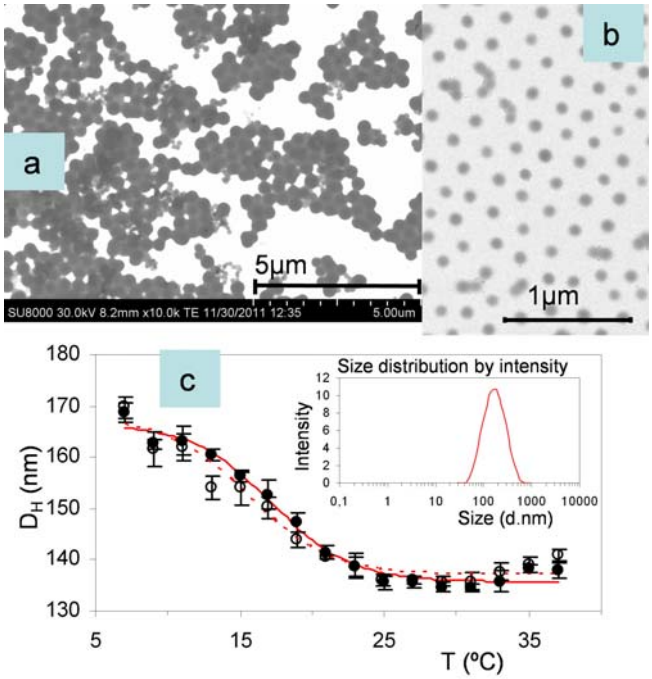
a
b
5µm
1µm
SU8000 30.0kV 8.2mm x10.0k TE 11/30/2011 12:35
5.00um
c
Size distribution by intensity
Intensity
Size (d.nm)
D_H (nm)
T (ºC)

Figure 2

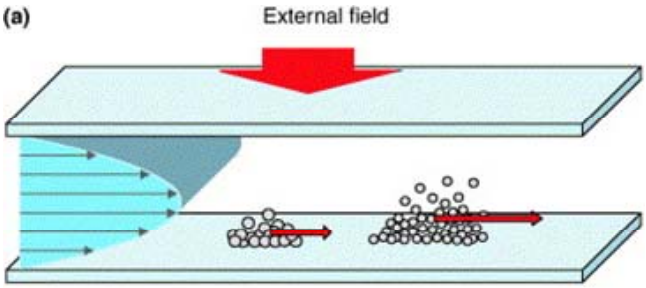

Figure 3

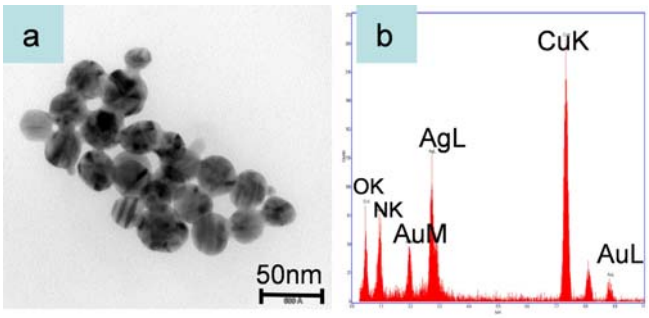

Figure 4

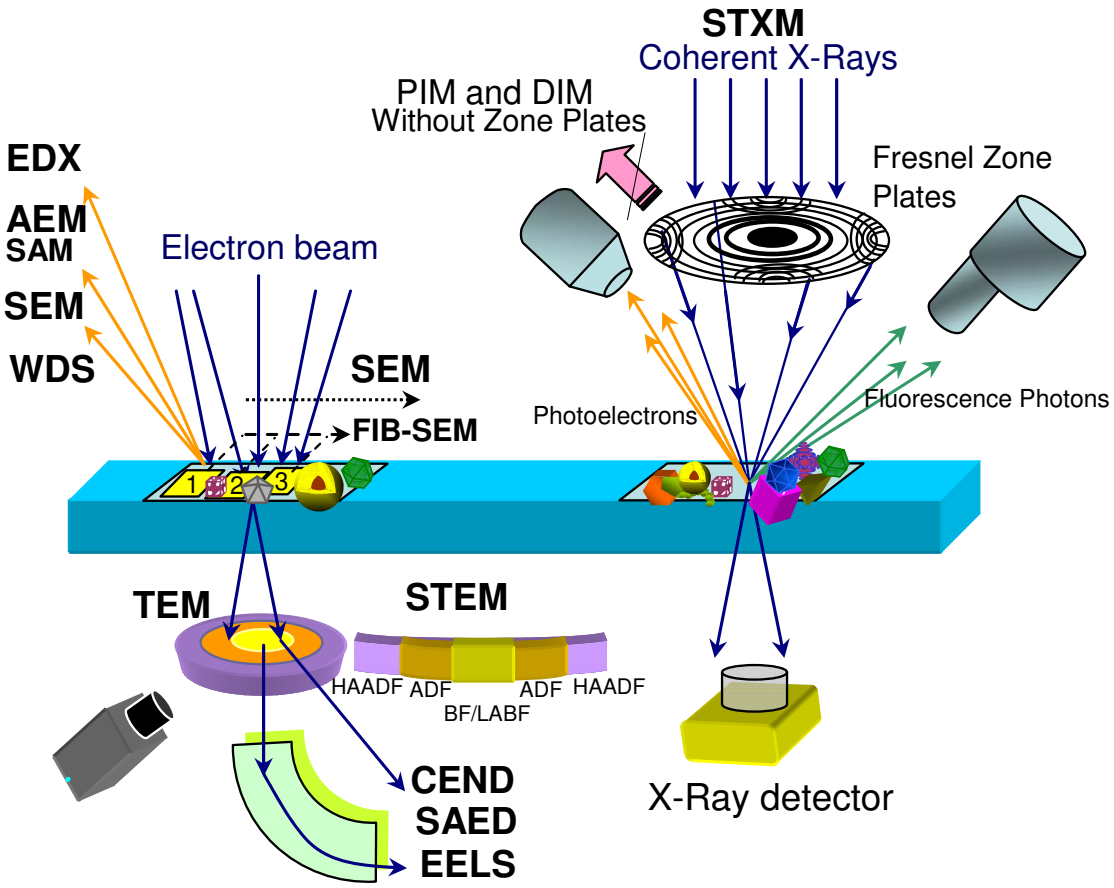
STXM
Coherent X-Rays
PIM and DIM
Without Zone Plates
Fresnel Zone
Plates
EDX
AEM
SAM
SEM
WDS
Electron beam
SEM
FIB-SEM
Photoelectrons
Fluorescence Photons
1
2
3
TEM
STEM
HAADF
ADF
ADF
HAADF
BF/LABF
CEND
SAED
EELS
X-Ray detector

Figure 5

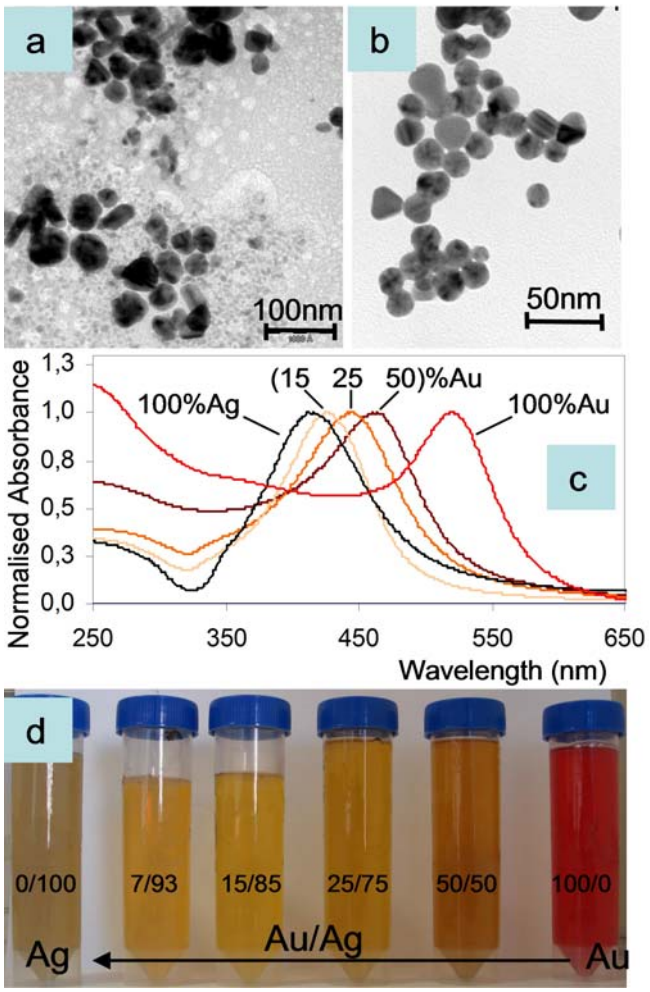
a
100nm
b
50nm
Normalised Absorbance
1,3
1,0
0,8
0,5
0,3
0,0
100%Ag
(15
25
50)%Au
100%Au
c
250
350
450
550
650
Wavelength (nm)
d
0/100
7/93
15/85
25/75
50/50
100/0
Ag
Au/Ag
Au

Figure 6

Reference List

1. Grolimund, D., Elimelech, M., Borkovec, M., Aggregation and deposition kinetics of mobile colloidal particles in natural porous media, *Colloids Surf. , A,* **191,** 179, (2001).

2. Badawy, A. M. E., Luxton, T. P., Silva, R. G., Scheckel, K. G., Suidan, M. T., Tolaymat, T. M., Impact of Environmental Conditions (pH, Ionic Strength, and Electrolyte Type) on the Surface Charge and Aggregation of Silver Nanoparticles Suspensions, *Environ. Sci. Technol.,* **44,** 1260, (2010).

3. Gong, J., Mullins, C. B., Surface Science Investigations of Oxidative Chemistry on Gold, *Acc. Chem. Res.,* **42,** 1063, (2009).

4. Kuchibhatla, S., Karakoti, A., Seal, S., Colloidal stability by surface modification, *JOM,* **57,** 52, (2005).

5. Jiang, J., Oberdorster, G., Elder, A., Gelein, R., Mercer, P., Biswas, P., Does Nanoparticle Activity Depend upon Size and Crystal Phase?, *Nanotoxicology,* **2,** 33, (2008).

6. Tiede, K., Tear, S. P., David, H., Boxall, A. B. A., Imaging of engineered nanoparticles and their aggregates under fully liquid conditions in environmental matrices, *Water Res,* **43,** 3335, (2009).

7. Alayoglu, S., Zavalij, P., Eichhorn, B., Wang, Q., Frenkel, A. I., Chupas, P., Structural and Architectural Evaluation of Bimetallic Nanoparticles: A Case Study of Pt−Ru Core−Shell and Alloy Nanoparticles, *ACS Nano,* **3,** 3127, (2009).

8. Borm, P., Robbins, D., Haubold, S., Kuhlbusch, T., Fissan, H., Donaldson, K., Schins, R., Stone, V., Kreyling, W., Lademann, J., Krutmann, J., Warheit, D., Oberdorster, E., The potential risks of nanomaterials: a review carried out for ECETOC, *Part Fibre Toxicol,* **3,** 11, (2006).

9. Tiede, K., Hassellöv, M., Breitbarth, E., Chaudhry, Q., Boxall, A. B. A., Considerations for environmental fate and ecotoxicity testing to support environmental risk assessments for engineered nanoparticles, *J. Chromatogr. , A,* **1216,** 503, (2009).

10. Alvarez, L., Siqueiros, J. M., Scanning Probe Microscopy, in *Microscopy: Science, Technology, Applications and Education,* A.Méndez-Vilas and J.Díaz, Eds., Formatex, 1302,(2010).

11. Oshikane, Y., Kataoka, T., Okuda, M., Hara, S., Inoue, H., Nakano, M., Observation of nanostructure by scanning near-field optical microscope with small sphere probe, *Sci. Technol. Adv. Mater.,* **8,** 181, (2007).

12. Johnson, T. W., Lapin, Z. J., Beams, R., Lindquist, N. C., Rodrigo, S. G., Novotny, L., Oh, S. H., Highly Reproducible Near-Field Optical Imaging with Sub-20-nm Resolution Based on Template-Stripped Gold Pyramids, *ACS Nano,* **6,** 9168, (2012).

13. Tiede, K., Boxall, A. B. A., Tear, S. P., Lewis, J., David, H., Hassellov, M., Detection and characterization of engineered nanoparticles in food and the environment, *Food Addit. Contam. , Part A,* **25,** 795, (2008).

14. Hak, S., Helgesen, E., Hektoen, H. H., Huuse, E. M., Jarzyna, P. A., Mulder, W. J. M., Haraldseth, O., Davies, C. d. L., The Effect of Nanoparticle Polyethylene Glycol Surface Density on Ligand-Directed Tumor Targeting Studied in Vivo by Dual Modality Imaging, *ACS Nano,* **6,** 5648, (2012).

15. Stephens, D. J., Allan, V. J., Light microscopy techniques for live cell imaging, *Science (New York, N. Y.),* **300,** 82, (2003).

16. Romero, G., Estrela-Lopis, I., Zhou, J., Rojas, E., Franco, A., Espinel, C. S., Fernández, A. G., Gao, C., Donath, E., Moya, S. E., Surface Engineered Poly(lactide-co-glycolide) Nanoparticles for Intracellular Delivery: Uptake and Cytotoxicity: A Confocal Raman Microscopic Study, *Biomacromolecules,* **11,** 2993, (2010).

17. Murphy, C. J., Gole, A. M., Stone, J. W., Sisco, P. N., Alkilany, A. M., Goldsmith, E. C., Baxter, S. C., Gold Nanoparticles in Biology: Beyond Toxicity to Cellular Imaging, *Acc. Chem. Res.,* **41,** 1721, (2008).

18. Xu, X. H. N., Brownlow, W. J., Kyriacou, S. V., Wan, Q., Viola, J. J., Real-Time Probing of Membrane Transport in Living Microbial Cells Using Single Nanoparticle Optics and Living Cell ImagingΓÇá, *Biochemistry,* **43,** 10400, (2004).

19. Domingos, R. F., Baalousha, M. A., Ju-Nam, Y., Reid, M. M., Tufenkji, N., Lead, J. R., Leppard, G. G., Wilkinson, K. J., Characterizing Manufactured Nanoparticles in the Environment: Multimethod Determination of Particle Sizes, *Environ. Sci. Technol.,* **43,** 7277, (2009).

20. Fatin-Rouge, N., Buffle, J., Study of Environmental Systems by Means of Fluorescence Correlation Spectroscopy, John Wiley & Sons, Ltd, 507,(2006).

21. Jurkiewicz, P., Konák, C., Subr, V., Hof, M., Stepánek, P., lbrich, K., Investigation of Nanoparticle Coating by Fluorescence Correlation Spectroscopy, *Macromol. Chem. Phys.,* **209,** 1447, (2008).

22. Ramirez-Aguilar, K. A., Lehmpuhl, D. W., Michel, A. E., Birks, J. W., Rowlen, K. L., Atomic force microscopy for the analysis of environmental particles, *Ultramicroscopy,* **77,** 187, (1999).

23. Mavrocordatos, D., Pronk, W., Boller, M., Analysis of environmental particles by atomic force microscopy, scanning and transmission electron microscopy, *Water Sci. Technol.,* **50,** 9, (2004).

24. Kaegi, R., Wagner, T., Hetzer, B., Sinnet, B., Tzvetkov, G., Boller, M., Size, number and chemical composition of nanosized particles in drinking water determined by analytical microscopy and LIBD, *Water Res.,* **42,** 2778, (2008).

25. Goodwin, J. W., Characterization of Colloidal Particles, John Wiley & Sons, Ltd, 195,(2004).

26. Hell, S. W., Far-Field Optical Nanoscopy, *Science,* **316,** 1153, (2007).

27. Betzig, E., Patterson, G. H., Sougrat, R., Lindwasser, O. W., Olenych, S., Bonifacino, J. S., Davidson, M. W., Lippincott-Schwartz, J., Hess, H. F., Imaging Intracellular Fluorescent Proteins at Nanometer Resolution, *Science,* **313,** 1642, (2006).

28. Dudkiewicz, A., Tiede, K., Boxall, A. B. A., Loeschner, K., Jensen, L. H. S., Jensen, E., Wierzbicki, R., Molhave, K., Characterization of nanomaterials in food by electron microscopy, *TrAC, Trends Anal. Chem.,* **30,** 28, (2011).

29. National Center for Electron Microscopy (NCEM)U.S.A.. availabe from http://ncem.lbl.gov/TEAM-project/files/what.html . 2010.

30. Kaneko, K., Inoke, K., Freitag, B., Hungria, A. B., Midgley, P. A., Hansen, T. W., Zhang, J., Ohara, S., Adschiri, T., Structural and Morphological Characterization of Cerium Oxide Nanocrystals Prepared by Hydrothermal Synthesis, *Nano Lett.,* **7,** 421, (2007).

31. Jefferson, D. A., Tilley, E. E. M., The structural and physical chemistry of nanoparticles, Particulate Matter - Properties and Effects on Health, Maynard, R. L. and Howard, C. V., Eds., Oxford, BIOS Scientific publishers, 63,(1999).

32. Koh, A. L., Shachaf, C. M., Elchuri, S., Nolan, G. P., Sinclair, R., Electron microscopy localization and characterization of functionalized composite organic-inorganic SERS nanoparticles on leukemia cells, *Ultramicroscopy,* **109,** 111, (2008).

33. Buhr, E., Senftleben, N., Klein, T., Bergmann, D., Gnieser, D., Frase, C. G., Bosse, H., Characterization of nanoparticles by scanning electron microscopy in transmission mode, *Meas. Sci. Technol,* **20,** 084025, (2009).

34. Klein, T., Buhr, E., Johnsen, K. P., Frase, C. G., Traceable measurement of nanoparticle size using a scanning electron microscope in transmission mode (TSEM), *Meas. Sci. Technol,* **22,** 094002, (2011).

35. Postek, M. T., Critical Issues in Scanning Electron Microscope Metrology, *Journal of Research of the National Institute of Standards and Technology,* **99,** 641, (1994).

36. Denk, W., Horstmann, H., Serial Block-Face Scanning Electron Microscopy to Reconstruct Three-Dimensional Tissue Nanostructure, *PLoS Biol,* **2,** e329, (2004).

37. Nanofabrication Using Focused Ion and Electron Beams: Principles and Applications, Oxford Series in Nanomanufacturing,(2012).

38. Liu, J., Scanning transmission electron microscopy and its application to the study of nanoparticles and nanoparticle systems, *J Electron Microsc,* **54,** 251, (2005).

39. Pennycook, S. J., Lupini, A. R., Varela, M., Borisevich, A. Y., Peng, Y., Oxley, M. P., Chisholm, M. F., Scanning Transmission Electron Microscopy for Nanostructure Characterization, in *Scanning Microscopy for Nanotechnology: Techniques and Applications,* Zhou, W. and Wang, Z. L., Eds., Springer, 152,(2006).

40. Nellist, P. D., McCallum, B. C., Rodenburg, J. M., Resolution beyond the 'information limit' in transmission electron microscopy, *Nature,* **374,** 630, (1995).

41. de Jonge, N., Ross, F. M., Electron microscopy of specimens in liquid, *Nat. Nano,* **6,** 695, (2011).

42. Hondow, N., Harrington, J., Brydson, R., Doak, S. H., Singh, N., Manshian, B., Brown, A., STEM mode in the SEM: A practical tool for nanotoxicology, *Nanotoxicology,* **5,** 215, (2010).

43. Huang, P. Y., Ruiz-Vargas, C. S., van der Zande, A. M., Whitney, W. S., Levendorf, M. P., Kevek, J. W., Garg, S., Alden, J. S., Hustedt, C. J., Zhu, Y., Park, J., McEuen, P. L., Muller, D. A., Grains and grain boundaries in single-layer graphene atomic patchwork quilts, *Nature,* **469,** 389, (2011).

44. Niels de Jonge, R. S., Nanotechnology in Biology and Medicine - Methods, Devices, and Applications, CRC Press, Boca Raton, FL, USA, 13,(2007).

45. Boyd, R., Young, T., Stolojan, V., Characterisation of gold nanoparticles and rods using high angle annular dark field imaging, *J. Nanopart. Res.,* **14,** 1, (2012).

46. Scott, M. C., Chen, C. C., Mecklenburg, M., Zhu, C., Xu, R., Ercius, P., Dahmen, U., Regan, B. C., Miao, J., Electron tomography at 2.4-angstrom resolution, *Nature,* **483,** 444, (2012).

47. Cowley, J. M., Merkulov, V. I., Lannin, J. S., Imaging of light-atom nanocrystals with a thin annular detector in STEM, *Ultramicroscopy,* **65,** 61, (1996).

48. Sousa, A. A., Hohmann-Marriott, M. F., Zhang, G., Leapman, R. D., Monte Carlo electron-trajectory simulations in bright-field and dark-field STEM: Implications for tomography of thick biological sections, *Ultramicroscopy,* **109,** 213, (2009).

49. Grogan, J. M., Bau, H. H., The Nanoaquarium: A Platform for In Situ Transmission Electron Microscopy in Liquid Media, *J. Microelectromech. Syst.,* **19,** 885, (2010).

50. Klein, K. L., Anderson, I. M., De Jonge, E. N., Transmission electron microscopy with a liquid flow cell, *J. Microsc,* **242,** 117, (2011).

51. Liu, K. L., Wu, C. C., Huang, Y. J., Peng, H. L., Chang, H. Y., Chang, P., Hsu, L., Yew, T. R., Novel microchip for in situ TEM imaging of living organisms and bio-reactions in aqueous conditions, *Lab Chip,* **8,** 1915, (2008).

52. Ryan, F., Morefield, S., Wen, J., Liao, D., Alvarado, J., Strano, M., Marsh, C., A Study of Nanomaterial Dispersion in Solution by Wet-Cell Transmission Electron Microscopy, *J. Nanosci. Nanotechnol.,* **8,** 4404, (2008).

53. Garg, P., Alvarado, J. L., Marsh, C., Carlson, T. A., Kessler, D. A., Annamalai, K., An experimental study on the effect of ultrasonication on viscosity and heat transfer performance of multi-wall carbon nanotube-based aqueous nanofluids, *Int. J. Heat Mass Transfer,* **52,** 5090, (2009).

54. Zheng, H., Smith, R. K., Jun, Y. w., Kisielowski, C., Dahmen, U., Alivisatos, A. P., Observation of Single Colloidal Platinum Nanocrystal Growth Trajectories, *Science,* **324,** 1309, (2009).

55. Yaguchi, T., Kanemura, T., Shimizu, T., Imamura, D., Watabe, A., Kamino, T., Development of a technique for in situ high temperature TEM observation of catalysts in a highly moisturized air atmosphere, *J. Electron Microsc.,* (2012).

56. Creemer JF, Santagata F, Morana B, Mele L, Alan T, Iervolino E, Pandraud G, Sarro PM. An all-in-one nanoreactor for high-resolution microscopy on nanomaterials at high pressures. Micro Electro Mechanical Systems (MEMS), 2011 IEEE 24th International Conference on. Micro.Electro.Mechanical.Systems (MEMS.), 2011.IEEE 24th.International.Conference on , 1103-1106. 23-1-2011.

57. Creemer, J. F., Helveg, S., Kooyman, P. J., Molenbroek, A. M., Zandbergen, H. W., Sarro, P. M., A MEMS Reactor for Atomic-Scale Microscopy of Nanomaterials Under Industrially Relevant Conditions, *J. Microelectromech. Syst,* **19,** 254, (2010).

58. Ring, E. A., de Jonge, N., Microfluidic System for Transmission Electron Microscopy, *Microsc. Microanal.,* **16,** 622, (2010).

59. Peckys, D. B., Veith, G. M., Joy, D. C., de Jonge, N., Nanoscale Imaging of Whole Cells Using a Liquid Enclosure and a Scanning Transmission Electron Microscope, *PLoS ONE,* **4,** e8214, (2009).

60. Evans, J. E., Jungjohann, K. L., Browning, N. D., Arslan, I., Controlled Growth of Nanoparticles from Solution with In Situ Liquid Transmission Electron Microscopy, *Nano Letters,* **11,** 2809, (2011).

61. Bogner, A., Thollet, G., Basset, D., Jouneau, P. H., Gauthier, C., Wet STEM: A new development in environmental SEM for imaging nano-objects included in a liquid phase, *Ultramicroscopy,* **104,** 290, (2005).

62. Doucet, F. J., Lead, J. R., Maguire, L., Achterberg, E. P., Millward, G. E., Visualisation of natural aquatic colloids and particles - a comparison of conventional high vacuum and environmental scanning electron microscopy, *J. Environ. Monit.,* **7,** 115, (2005).

63. Stokes, D. J., Baken, E., Electron Microscopy of Soft Nano-materials, *I. &M.,* **9,** 18, (2007).

64. Gatti, A., Kirkpatrick, J., Gambarelli, A., Capitani, F., Hansen, T., Eloy, R., Clermont, G., ESEM evaluations of muscle/nanoparticles interface in a rat model, *J. Mater. Sci. - Mater. Med.,* **19,** 1515, (2008).

65. Giorgio, S., Sao Joao, S., Nitsche, S., Chaudanson, D., Sitja, G., Henry, C. R., Environmental electron microscopy (ETEM) for catalysts with a closed E-cell with carbon windows, *Ultramicroscopy,* **106,** 503, (2006).

66. Kishita, K., Sakai, H., Tanaka, H., Saka, H., Kuroda, K., Sakamoto, M., Watabe, A., Kamino, T., Development of an analytical environmental TEM system and its application, *J. Electron Microsc.,* **58,** 331, (2009).

67. Timp, W., Watson, N., Sabban, A., Zik, O., Matsudaira, P., Wet electron microscopy with quantum dots., *Biotechniques,* **41,** 295, (2006).

68. Balmes, O., Malm, J. O., Pettersson, N., Karlsson, G., Bovin, J. O., Imaging Atomic Structure in Metal Nanoparticles Using High-Resolution Cryo-TEM, *Microsc. Microanal.,* **12,** 145, (2006).

69. Anjum, D. H., Stiger, R. M., Finley, J. J., Conway, J. F., Cryo-transmission electron microscopy of Ag nanoparticles grown on an ionic liquid substrate, *J. Mater. Res,* **25,** 1264, (2010).

70. Hu, M., Qian, L., Briñas, R. P., Lymar, E. S., Kuznetsova, L., Hainfeld, J. F., Gold nanoparticle-protein arrays improve resolution for cryo-electron microscopy, *J. Struct. Biol.,* **161,** 83, (2008).

71. Wang, Y., Zeiri, O., Gitis, V., Neyman, A., Weinstock, I. A., Reversible binding of an inorganic cluster-anion to the surface of a gold nanoparticle, *Inorg. Chim. Acta,* **363,** 4416, (2010).

72. Luo, H., Scriven, L. E., Francis, L. F., Cryo-SEM studies of latex/ceramic nanoparticle coating microstructure development, *J. Colloid Interface Sci.,* **316,** 500, (2007).

73. Murphy, G. E., Jensen, G. J., Electron Cryotomography, *Biotechniques,* **43,** 413, (2007).

74. Nel, A. E., Madler, L., Velegol, D., Xia, T., Hoek, E. M. V., Somasundaran, P., Klaessig, F., Castranova, V., Thompson, M., Understanding biophysicochemical interactions at the nano-bio interface, *Nat Mater,* **8,** 543, (2009).

75. Taveau, J. C., Nguyen, D., Perro, A., Ravaine, S., Duguet, E., Lambert, O., New insights into the nucleation and growth of PS nodules on silica nanoparticles by 3D cryo-electron tomography, *Soft Matter,* **4,** 311, (2008).

76. Lengyel, J. S., Milne, J. L., Subramaniam, S., Electron tomography in nanoparticle imaging and analysis, *Nanomedicine,* **3,** 125, (2008).

77. Le Bihan, O., Bonnafous, P., Marak, L., Bickel, T., Trθpout, S., Mornet, S., De Haas, F., Talbot, H., Taveau, J. C., Lambert, O., Cryo-electron tomography of nanoparticle transmigration into liposome, *J. Struct. Biol.,* **168,** 419, (2009).

78. Balnois, E., Papastavrou, G., Wilkinson, K. J., Force Microscopy and Force Measurements of Environmental Colloids, John Wiley & Sons, Ltd, 405,(2006).

79. Solid State Characterization of Pharmaceuticals, Wiley,(2011).

80. Nanoparticle Technology: Handbook, Elsevier,(2012).

81. Zhong, Q., Inniss, D., Kjoller, K., Elings, V. B., Fractured polymer/silica fiber surface studied by tapping mode atomic force microscopy, *Surf. Sci. Lett.,* **290,** L688-L692, (1993).

82. Keller, D., Bustamante, C., Attaching molecules to surfaces for scanning probe microscopy, *Biophys. J .,* **64,** 896, (1993).

83. Lead, J. R., Muirhead, D., Gibson, C. T., Characterization of Freshwater Natural Aquatic Colloids by Atomic Force Microscopy (AFM), *Environ. Sci. Technol.,* **39,** 6930, (2005).

84. Muirhead, D., Lead, J. R., Measurement of the size and structure of natural aquatic colloids in an urbanised watershed by atomic force microscopy, *Hydrobiologia,* **494,** 65, (2003).

85. Doucet, F. J., Maguire, L., Lead, J. R., Size fractionation of aquatic colloids and particles by cross-flow filtration: analysis by scanning electron and atomic force microscopy, *Anal. Chim. Acta,* **522,** 59, (2004).

86. Baalousha, M., Lead, J. R., Size fractionation and characterization of natural aquatic colloids and nanoparticles, *Sci. Total Environ.,* **386,** 93, (2007).

87. Rao, A., Schoenenberger, M., Gnecco, E., Glatzel, Th., Meyer, E., Brändlin, D., Scandella, L., Characterization of nanoparticles using Atomic Force Microscopy, *Journal of Physics: Conference Series,* **61,** 971, (2007).

88. Suenne Kim, Farbod Shafiei, Daniel Ratchford, Xiaoqin Li, Controlled AFM manipulation of small nanoparticles and assembly of hybrid nanostructures, *Nanotechnology,* **22,** 115301, (2011).

89. Guo, D., Wu, C., Li, X., Jiang, H., Wang, X., Chen, B., In Vitro Cellular Uptake and Cytotoxic Effect of Functionalized Nickel Nanoparticles on Leukemia Cancer Cells, *J. Nanosci. Nanotechnol.,* **8,** 2301, (2008).

90. Contreras-Cáceres, R., Pacifico, J., Pastoriza-Santos, I., Pérez-Juste, J., Fernández-Barbero, A., Liz-Marzán, L. M., Au@pNIPAM Thermosensitive Nanostructures: Control over Shell Cross-linking, Overall Dimensions, and Core Growth, *Adv. Funct. Mater.,* **19,** 3070, (2009).

91. Le Gros, M. A., McDermott, G., Larabell, C. A., X-ray tomography of whole cells, *Curr Opin Struct Biol,* **15,** 593, (2005).

92. Takahashi, Y., Zettsu, N., Nishino, Y., Tsutsumi, R., Matsubara, E., Ishikawa, T., Yamauchi, K., Three-Dimensional Electron Density Mapping of Shape-Controlled Nanoparticle by Focused Hard X-ray Diffraction Microscopy, *Nano Lett.,* **10,** 1922, (2010).

93. Nelson, J., Huang, X., Steinbrener, J., Shapiro, D., Kirz, J., Marchesini, S., Neiman, A. M., Turner, J. J., Jacobsen, C., High-resolution x-ray diffraction microscopy of specifically labeled yeast cells, *PNAS,* (2010).

94. Newton, M. C., Leake, S. J., Harder, R., Robinson, I. K., Three-dimensional imaging of strain in a single ZnO nanorod, *Nat Mater,* **9,** 120, (2010).

95. Pfeifer, M. A., Williams, G. J., Vartanyants, I. A., Harder, R., Robinson, I. K., Three-dimensional mapping of a deformation field inside a nanocrystal, *Nature,* **442,** 63, (2006).

96. Xiaojin, G., Huang, X., Leake, S., Newton, M. C., Harder, R., Robinson, I. K., Coherent x-ray diffraction imaging of ZnO nanostructures under confined illumination, *New J. Phys,* **13,** 033006, (2011).

97. Isaacs, E. D., Microscopy: X-ray nanovision, *Nature,* **442,** 35, (2006).

98. Yang, W., Huang, X., Harder, R., Clark, J. N., Robinson, I. K., Mao, H. k., Coherent diffraction imaging of nanoscale strain evolution in a single crystal under high pressure, *Nat. Commun.,* **4,** 1680, (2013).

99. Thieme, J., McNult, I., Vogt, S., Paterson, a. D., X-Ray Spectromicroscopy A Tool for Environmental Sciences, *Environ. Sci. Technol.,* **41,** 6885, (2007).

100. Myneni, S. C. B., Brown, J. T., Martinez, G. A., Meyer-Ilse, W., Imaging of Humic Substance Macromolecular Structures in Water and Soils, *Science,* **286,** 1335, (1999).

101. Kuo, C. H., Chu, Y. T., Song, Y. F., Huang, M. H., Cu2O Nanocrystal-Templated Growth of Cu2S Nanocages with Encapsulated Au Nanoparticles and In-Situ Transmission X-ray Microscopy Study, *Adv. Funct. Mater.,* **21,** 792, (2011).

102. Auernhammer, G. K., Fauth, K., Ullrich, B., Zhao, J., Weigand, M., Vollmer, D., Time-resolved X-ray microscopy of nanoparticle aggregates under oscillatory shear, *J Synchrotron Radiat,* **16,** 307, (2009).

103. Burke, K. B., Staplenton, A. J., Vaughan, B., Zhou, X., Kilcoyne, A. L. D., Belcher, W. J., Dastoor, P. C., Scanning transmission x-ray microscopy of polymer nanoparticles: probing morphology on sub-10-nm length scales, *Nanotechnology,* **22,** 265710, (2011).

104. Robinson, I., Harder, R., Coherent X-ray diffraction imaging of strain at the nanoscale, *Nat. Mater.,* **8,** 291, (2009).

105. Chapman, H. N., X-ray imaging beyond the limits, *Nat. Mater.,* **8,** 299, (2009).

106. Chao, W., Harteneck, B. D., Liddle, J. A., Anderson, E. H., Attwood, D. T., Soft X-ray microscopy at a spatial resolution better than 15 nm, *Nature,* **435,** 1210, (2005).

107. Benk, M., Bergmann, K., Querejeta-Fernandez, A., Srivastava, S., Kotov, N. A., Schaefer, D., Wilheim, T., Soft X-Ray Microscopic Investigation on Self Assembling Nanocrystals, *AIP Conf. Proc.,* **1365,** 433, (2011).

108. Nilsson, H., Tyliszczak, T., Wilson, R., Werme, L., Shuh, D., Soft X-ray scanning transmission X-ray microscopy (STXM) of actinide particles, *Anal. Bioanal. Chem.,* **383,** 41, (2005).

109. Brar, S. K., Verma, M., Measurement of nanoparticles by light-scattering techniques, *TrAC, Trends Anal. Chem.,* **30,** 4, (2011).

110. Bootz, A., Vogel, V., Schubert, D., Kreuter, J. r., Comparison of scanning electron microscopy, dynamic light scattering and analytical ultracentrifugation for the sizing of poly(butyl cyanoacrylate) nanoparticles, *Eur. J. Pharm. Biopharm.,* **57,** 369, (2004).

111. Hassellöv, M., Readman, J., Ranville, J., Tiede, K., Nanoparticle analysis and characterization methodologies in environmental risk assessment of engineered nanoparticles, *Ecotoxicology,* **17,** 344, (2008).

112. Finsy, R., Particle sizing by quasi-elastic light scattering, *Adv. Colloid Interface Sci.,* **52,** 79, (1994).

113. Panáek, A., Krvítek, L., Prucek, R., Kolár M., Veerová, R., Pizúrová, N., Virender K.Sharma, V., Nevená, T., Zboril, R., Silver Colloid Nanoparticles: Synthesis, Characterization, and Their Antibacterial Activity, *J. Phys. Chem. B,* **110,** 16248, (2006).

114. Yu, L., Andriola, A., Quantitative gold nanoparticle analysis methods: A review, *Talanta,* **82,** 869, (2010).

115. Lapresta-Fernández, A., Doussineau, T., Dutz, S., Steiniger, F., Moro, A. J., Mohr, G. J., Magnetic And Fluorescent Core-Shell Nanoparticles For Ratiometric pH Sensing, *Nanotechnology,* **22,** 415501(10 pp), (2011).

116. Lapresta-Fernández, A., Doussineau, T., Moro, A. J., Dutz, S., Steiniger, F., Mohr, G. J., Magnetic core-shell fluorescent ph ratiometric nanosensor using a Stöber coating method, *Anal. Chim. Acta,* **707,** 164, (2011).

117. Lapresta-Fernández, A., Cywinski, P., Moro, A., Mohr, G., Fluorescent polyacrylamide nanoparticles for naproxen recognition, *Anal. Bioanal. Chem.,* **395,** 1821, (2009).

118. Urena-Benavides, E. E., Kitchens, C. L., of triaxial nanoparticle suspensions in the Rayleigh-Gans-Debye regime: application to cellulose nanocrystals, *RSC Adv.,* **2,** 1096, (2012).

119. Jung, E., Cho, H. R., Park, K., Yeon, J. W., Song, K., Nanoparticle sizing by a laser-induced breakdown detection using an optical probe beam deflection, *Appl. Phys. B-Lasers O,* **97,** 867, (2009).

120. Latkoczy, C., Kagi, R., Fierz, M., Ritzmann, M., Gunther, D., Boller, M., Development of a mobile fast-screening laser-induced breakdown detection (LIBD) system for field-based measurements of nanometre sized particles in aqueous solutions, *J. Environ. Monit.,* **12,** 1422, (2010).

121. Mueller, M., Gornushkin, I. B., Florek, S., Mory, D., Panne, U., Approach to Detection in Laser-Induced Breakdown Spectroscopy, *Anal. Chem.,* **79,** 4419, (2007).

122. Tiwari, V. S., Oleg, T., Darbha, G. K., Hardy, W., Singh, J. P., Ray, P. C., Non-resonance SERS effects of silver colloids with different shapes, *Chem. Phys. Lett.,* **446,** 77, (2007).

123. Ming Li and Scott, Shape-dependent surface-enhanced Raman scattering in gold–Raman-probe–silica sandwiched nanoparticles for biocompatible applications, *Nanotechnology,* **23,** 115501, (2012).

124. Qian, X., Peng, X. H., Ansari, D. O., Yin-Goen, Q., Chen, G. Z., Shin, D. M., Yang, L., Young, A. N., Wang, M. D., Nie, S., In vivo tumor targeting and spectroscopic detection with surface-enhanced Raman nanoparticle tags, *Nat Biotech,* **26,** 83, (2008).

125. Tsoutsi, D., Montenegro, J. M., Dommershausen, F., Koert, U., Liz-Marzán, L. M., Parak, W. J., Álvarez-Puebla, R. A., Quantitative Surface-Enhanced Raman Scattering Ultradetection of Atomic Inorganic Ions: The Case of Chloride, *ACS Nano,* **5,** 7539, (2011).

126. Jimenez de Aberasturi, D., Montenegro, J. M., Ruiz de Larramendi, I., Rojo, T., Klar, T. A., Álvarez-Puebla, R., Liz-Marzán, L. M., Parak, W. J., Optical Sensing of Small Ions with Colloidal Nanoparticles, *Chem. Mater.,* **24,** 738, (2012).

127. Álvarez-Puebla, R. A., Agarwal, A., Manna, P., Khanal, B. P., Aldeanueva-Potel, P., Carbó Argibay, E., Pazos-Pérez, N., Vigderman, L., Zubarev, E. R., Kotov, N. A., Liz-Marzán, L. M., Gold nanorods 3D-supercrystals as surface enhanced Raman scattering spectroscopy substrates for the rapid detection of scrambled prions, *PNAS,* **108,** 8157, (2011).

128. Nakamura, K., Kawabata, T., Mori, Y., Size distribution analysis of colloidal gold by small angle X-ray scattering and light absorbance, *Powder Technol.,* **131,** 120, (2003).

129. Wellsted, H., Sitsen, E., Caragheorgheopol, A., Chechik, V., Polydisperse Composition of Mixed Monolayer-Protected, Spin-Labeled Au Nanoparticles, *Anal. Chem.,* **76,** 2010, (2004).

130. Link, S., El-Sayed, M. A., Shape and size dependence of radiative, non-radiative and photothermal properties of gold nanocrystals, *Int Rev Phys Chem,* **19,** 409, (2000).

131. Yu, C., Irudayaraj, J., Multiplex Biosensor Using Gold Nanorods, *Anal Chem,* **79,** 572, (2006).

132. Hu, M., Chen, J., Li, Z. Y., Au, L., Hartland, G. V., Li, X., Marquez, M., Xia, Y., Gold nanostructures: engineering their plasmonic properties for biomedical applications, *Chem. Soc. Rev.,* **35,** 1084, (2006).

133. Mannelli, I., Marco, M. P., Recent advances in analytical and bioanalysis applications of noble metal nanorods, *Anal Bioanal Chem,* **398,** 2451, (2010).

134. Blom, M. T., Chmela, E., Oosterbroek, R. E., Tijssen, R., van den Berg, A., On-Chip Hydrodynamic Chromatography Separation and Detection of Nanoparticles and Biomolecules, *Anal. Chem.,* **75,** 6761, (2003).

135. Wei, G. T., Liu, F. K., Separation of nanometer gold particles by size exclusion chromatography, *J. Chromatogr. , A,* **836,** 253, (1999).

136. Dubascoux, S., Von der Kammer, F., Le Hécho, I., Gautier, M. P., Lespes, G., Optimisation of asymmetrical flow field flow fractionation for environmental nanoparticles separation, *J. Chromatogr. , A,* **1206,** 160, (2008).

137. Polte, J., Erler, R., Thüenemann, A. F., Sokolov, S., Ahner, T. T., Rademann, K., Emmerling, F., Kraehnert, R., Nucleation and Growth of Gold Nanoparticles Studied via in situ Small Angle X-ray Scattering at Millisecond Time Resolution, *ACS Nano,* **4,** 1076, (2010).

138. Gomez, M. V., Guerra, J., Myers, V. S., Crooks, R. M., Velders, A. H., Nanoparticle Size Determination by 1H NMR Spectroscopy, *J. Am. Chem. Soc.,* **131,** 14634, (2009).

139. Follens, L. R. A., Aerts, A., Haouas, M., Caremans, T. P., Loppinet, B., Goderis, B., Vermant, J., Taulelle, F., Martens, J. A., Kirschhock, C. E. A., Characterization of nanoparticles in diluted clear solutions for Silicalite-1 zeolite synthesis using liquid 29Si NMR, SAXS and DLS, *Phys. Chem. Chem. Phys.,* **10,** 5574, (2008).

140. Moller, J., Cebi, M., Schroer, M. A., Paulus, M., Degen, P., Sahle, C. J., Wieland, D. C. F., Leick, S., Nyrow, A., Rehage, H., Tolan, M., Dissolution of iron oxide nanoparticles inside polymer nanocapsules, *Phys. Chem. Chem. Phys.,* **13,** 20354, (2011).

141. Gleber, G., Cibik, L., Haas, S., Hoell, A., Müller, P., Krumrey, M., Traceable size determination of PMMA nanoparticles based on Small Angle X-ray Scattering (SAXS), *Journal of Physics: Conference Series,* **247,** 012027, (2010).

142. Krumrey, M., Gleber, G., Scholze, F., Wernecke, J., Synchrotron radiation-based x-ray reflection and scattering techniques for dimensional nanometrology, *Meas. Sci. Technol.,* **22,** 094032, (2011).

143. Y.Mori, M.Furukawa, T.Hayashi, K.Nakamura, Size Distribution of Gold Nanoparticles Used by Small Angle X-ray Scattering, *Part. Sci. Technol.,* **24,** 97, (2006).

144. Hino, K., Shingai, R., Morita, T., Toku, K., Hirano, T., Yoshikawa, H., Nakano, H., Nishi, N., Size distribution of gold nanoparticles covered with thiol-terminated cyanobiphenyl-type liquid crystal molecules studied with small-angle X-ray scattering and TEM, *Chem. Phys. Lett.,* **460,** 173, (2008).

145. Bienert, R., Emmerling, F., Thünemann, A., The size distribution of 'gold standard' nanoparticles, *Anal. Bioanal. Chem.,* **395,** 1651, (2009).

146. Krycka, K. L., Booth, R. A., Hogg, C. R., Ijiri, Y., Borchers, J. A., Chen, W. C., Watson, S. M., Laver, M., Gentile, T. R., Dedon, L. R., Harris, S., Rhyne, J. J., Majetich, S. A., Core-Shell Magnetic Morphology of Structurally Uniform Magnetite Nanoparticles, *Phys. Rev. Lett.,* **104,** 207203, (2010).

147. Von White, G., Kitchens, C. L., Small-Angle Neutron Scattering of Silver Nanoparticles in Gas-Expanded Hexane, *J. Phys. Chem. C,* **114,** 16285, (2010).

148. Wang, S. H., Sun, Y. S., Chiang, A. S.-T., Hung, H. F., Chen, M. C., Wood, K., Carboxylic Acid-Directed Clustering and Dispersion of ZrO2 Nanoparticles in Organic Solvents: A Study by Small-Angle X-ray/Neutron Scattering and NMR, *J. Phys. Chem. C,* **115,** 11941, (2011).

149. Barth, H. G., Boyes, B. E., Size exclusion chromatography, *Anal. Chem.,* **64,** 428R, (1992).

150. Weinberg, H., Galyean, A., Leopold, M., Evaluating engineered nanoparticles in natural waters, *TrAC, Trends Anal. Chem.,* **30,** 72, (2011).

151. Liu, F. K., SEC Characterization of Au Nanoparticles Prepared through Seed-Assisted Synthesis, *Chromatographia,* **66,** 791, (2007).

152. Liu, F. K., Wei, G. T., Effect of Mobile-Phase Additives on Separation of Gold Nanoparticles by Size-Exclusion Chromatography, *Chromatographia,* **59,** 115, (2004).

153. Porsch, B., Welinder, A., K÷rner, A., Wittgren, B., Distribution analysis of ultra-high molecular mass poly(ethylene oxide) containing silica particles by size-exclusion chromatography with dual light-scattering and refractometric detection, *J. Chromatogr. , A,* **1068,** 249, (2005).

154. Al-Somali, A. M., Krueger, K. M., Falkner, J. C., Colvin, V. L., Recycling Size Exclusion Chromatography for the Analysis and Separation of Nanocrystalline Gold, *Anal. Chem.,* **76,** 5903, (2004).

155. Wei, G. T., Liu, F. K., Wang, C. R. C., Shape Separation of Nanometer Gold Particles by Size-Exclusion Chromatography, *Anal. Chem.,* **71,** 2085, (1999).

156. Small, H., Langhorst, M. A., Hydrodynamic chromatography, *Anal. Chem.,* **54,** 892A, (1982).

157. Williams, A., Varela, E., Meehan, E., Tribe, K., Characterisation of nanoparticulate systems by hydrodynamic chromatography, *Int. J. Pharm.,* **242,** 295, (2002).

158. Liu, J. f., Yu, S. j., Yin, Y. g., Chao, J. b., Methods for separation, identification, characterization and quantification of silver nanoparticles, *TrAC, Trends Anal. Chem.,* **33,** 95, (2012).

159. McGowan, G. R., Langhorst, M. A., Development and application of an integrated, high-speed, computerized hydrodynamic chromatograph, *J. Colloid Interface Sci.,* **89,** 94, (1982).

160. Yegin, B. A., Lamprecht, A., Lipid nanocapsule size analysis by hydrodynamic chromatography and photon correlation spectroscopy, *Int. J. Pharm.,* **320,** 165, (2006).

161. Chmela, E., Tijssen, R., Blom, M. T., Gardeniers, H. J. G. E., van den Berg, A., A Chip System for Size Separation of Macromolecules and Particles by Hydrodynamic Chromatography, *Anal. Chem.,* **74,** 3470, (2002).

162. Tiede, K., Boxall, A. B. A., Tiede, D., Tear, S. P., David, H., Lewis, J., A robust size-characterisation methodology for studying nanoparticle behaviour in 'real'

environmental samples, using hydrodynamic chromatography coupled to ICP-MS, *J. Anal. At. Spectrom.,* **24,** 964, (2009).

163. Liu, F. K., Chang, Y. C., Using reversed-phase liquid chromatography to monitor the sizes of Au/Pt core/shell nanoparticles, *J. Chromatogr. , A,* **1217,** 1647, (2010).

164. Song, Y., Heien, M. L., Jimenez, V., Wightman, R. M., Murray, R. W., Voltammetric Detection of Metal Nanoparticles Separated by Liquid Chromatography, *Anal. Chem.,* **76,** 4911, (2004).

165. Pyell, U., Characterization of nanoparticles by capillary electromigration separation techniques, *ELECTROPHORESIS,* **31,** 814, (2010).

166. López-Lorente, A. I., Simonet, B. M., Valcárcel, M., Electrophoretic methods for the analysis of nanoparticles, *TrAC, Trends Anal. Chem.,* **30,** 58, (2011).

167. Lo, C. K., Paau, M. C., Xiao, D., Choi, M. M. F., Application of capillary zone electrophoresis for separation of water-soluble gold monolayer-protected clusters, *Eletrophoresis,* **29,** 2330, (2008).

168. Lin, K. H., Chu, T. C., Liu, F. K., On-line enhancement and separation of nanoparticles using capillary electrophoresis, *J. Chromatogr. , A,* **1161,** 314, (2007).

169. Helfrich, A., Bruchert, W., Bettmer, J., Size characterisation of Au nanoparticles by ICP-MS coupling techniques, *J. Anal. At. Spectrom.,* **21,** 431, (2006).

170. Surugau, N., Urban, P., Electrophoretic methods for separation of nanoparticles., *J Sep Sci.,* **32,** 1889, (2009).

171. Liu, F. K., Analysis and applications of nanoparticles in the separation sciences: A case of gold nanoparticles, *J. Chromatogr. , A,* **1216,** 9034, (2009).

172. Buffle, J., Leppard, G. G., Characterization of Aquatic Colloids and Macromolecules. 2. Key Role of Physical Structures on Analytical Results, *Environ. Sci. Technol.,* **29,** 2176, (1995).

173. Giddings, J. C., Field-flow fractionation: analysis of macromolecular, colloidal, and particulate materials, *Science,* **260,** 1456, (1993).

174. Reschiglian, P., Zattoni, A., Roda, B., Michelini, E., Roda, A., Field-flow fractionation and biotechnology, *Trends Biotechnol.,* **23,** 475, (2005).

175. Messaud, F. A., Sanderson, R. D., Runyon, J. R., Otte, T., Pasch, H., Williams, S. K. R., An overview on field-flow fractionation techniques and their applications in the separation and characterization of polymers, *Progress. in Polymer Science,* **34,** 351, (2009).

176. Hassellöv, M., der Kammer, F. v., Beckett, R., Characterisation of Aquatic Colloids and Macromolecules by Field-Flow Fractionation, John Wiley & Sons, Ltd, 223,(2006).

177. Wyatt, P. J., Submicrometer Particle Sizing by Multiangle Light Scattering following Fractionation, *J. Colloid Interface Sci.,* **197,** 9, (1998).

178. Kammer, F., Baborowski, M., Friese, K., Field-flow fractionation coupled to multi-angle laser light scattering detectors: Applicability and analytical benefits for the analysis of environmental colloids, *Anal. Chim. Acta,* **552,** 166, (2005).

179. Baalousha, M., Kammer, F. V. D., Motelica-Heino, M., Le Coustumer, P., Natural sample fractionation by FlFFF-MALLS-TEM: Sample stabilization, preparation, pre-concentration and fractionation, *J. Chromatogr. , A,* **1093,** 156, (2005).

180. Sermsri, W., Jarujamrus, P., Shiowatana, J., Siripinyanond, A., Flow field-flow fractionation: a versatile approach for size characterization of α-tocopherol-induced enlargement of gold nanoparticles, *Anal. Bioanal. Chem.,* **396,** 3079, (2010).

181. Pace, H. E., Lesher, E. K., Ranville, J. F., Influence of stability on the acute toxicity of CdSe/ZnS nanocrystals to Daphnia magna, *Environ. Toxicol. Chem.,* **29,** 1338, (2010).

182. Field-Flow Fractionation in Biopolymer Analysis, Springer,(2012).

183. Moon, M. H., Kang, D., Jung, J., Kim, J., Separation of carbon nanotubes by frit inlet asymmetrical flow field-flow fractionation, *J. Sep. Science,* **27,** 710, (2004).

184. Bouby, M., Geckeis, H., Geyer, F. W., Application of asymmetric flow field-flow fractionation (AsFlFFF) coupled to inductively coupled plasma mass spectrometry (ICPMS) to the quantitative characterization of natural colloids and synthetic nanoparticles, *Anal Bioanal Chem,* **392,** 1447, (2008).

185. Klaine, S. J., Alvarez, P. J. J., Batley, G. E., Fernandes, T. F., Handy, R. D., Lyon, D. Y., Mahendra, S., McLaughlin, M. J., Lead, J. R., Nanomaterials in the environment: Behavior, fate, bioavailability, and effects, *Environ. Toxicol. Chem.,* **27,** 1825, (2008).

186. Machtle, W., Borger, L., Analytical Ultracentrifugation of Polymers and Nanoparticles, Berlin,(2006).

187. Colfen, H., Analysis of Nanoparticles <10 nm by Analytical Ultracentrifugation, in *Particle Sizing and Characterization,* American Chemical Society, 119,(2004).

188. Lead, J. R., Wilkinson, K. J., Aquatic Colloids and Nanoparticles: Current Knowledge and Future Trends, *Environ. Chem.,* **3,** 159, (2006).

189. Gimbert, L. J., Haygarth, P. M., Beckett, R., Worsfold, P. J., Comparison of Centrifugation and Filtration Techniques for the Size Fractionation of Colloidal Material in Soil Suspensions Using Sedimentation Field-Flow Fractionation, *Environ. Sci. Technol.,* **39,** 1731, (2005).

190. Morrison, M. A., Benoit, G., Filtration Artifacts Caused by Overloading Membrane Filters, *Environ. Sci. Technol.,* **35,** 3774, (2001).

191. Liu, R., Lead, J. R., Partial Validation of Cross Flow Ultrafiltration by Atomic Force Microscopy, *Anal. Chem.,* **78,** 8105, (2006).

192. Franklin, N. M., Rogers, N. J., Apte, S. C., Batley, G. E., Gadd, G. E., Casey, P. S., Comparative Toxicity of Nanoparticulate ZnO, Bulk ZnO, and ZnCl2 to a Freshwater Microalga (Pseudokirchneriella subcapitata): The Importance of Particle Solubility, *Environ. Sci. Technol.,* **41,** 8484, (2007).

193. Lu, S. G., Zheng, Y. W., Bai, S. Q., A HRTEM/EDX approach to identification of the source of dust particles on urban tree leaves, *Atmos. Environ.,* **42,** 6431, (2008).

194. Teng, X., Yang, H., Synthesis of Face-Centered Tetragonal FePt Nanoparticles and Granular Films from Pt@Fe2O3 Core-Shell Nanoparticles, *J. Am. Chem. Soc.,* **125,** 14559, (2003).

195. Feng, Q. L., Wu, J., Chen, G. Q., Cui, F. Z., Kim, T. N., Kim, J. O., A mechanistic study of the antibacterial effect of silver ions on Escherichia coli and Staphylococcus aureus, *J. Biomed. Mater. Res.,* **52,** 662, (2000).

196. Yang, J., Yang, J., Ying, J. Y., Morphology and Lateral Strain Control of Pt Nanoparticles via Core-Shell Construction Using Alloy AgPd Core Toward Oxygen Reduction Reaction, *ACS Nano,* **6,** 9373, (2012).

197. Haveli, S. D., Walter, P., Patriarche, G., Ayache, J., Castaing, J., Van Elslande, E., Tsoucaris, G., Wang, P. A., Kagan, H. B., Hair Fiber as a Nanoreactor in Controlled Synthesis of Fluorescent Gold Nanoparticles, *Nano Lett.,* **12,** 6212, (2012).

198. He, Y. F., Feng, J. T., Du, Y. Y., Li, D. Q., Controllable Synthesis and Acetylene Hydrogenation Performance of Supported Pd Nanowire and Cuboctahedron Catalysts, *ACS Catal.,* **2,** 1703, (2012).

199. Lyman, C. E., Williams, D. B., Goldstein, J. I., X-ray detectors and spectrometers, *Ultramicroscopy,* **28,** 137, (1989).

200. Tanaka, M., Takeguchi, M., Furuya, K., Wavelength dispersive X-ray spectroscopy of thick and thin samples for electron microscopes, *Surf. Interface Anal.,* **40,** 1684, (2008).

201. Bogle, K. A., Anbusathaiah, V., Arredondo, M., Lin, J. Y., Chu, Y. H., O´Neil, C., Gregg, J. M., Castell, M. R., Nagarajan, V., Synthesis of Epitaxial Metal Oxide Nanocrystals via a Phase Separation Approach, *ACS Nano,* **4,** 5139, (2010).

202. Yin, J., Shan, S., Yang, L., Mott, D., Malis, O., Petkov, V., Cai, F., Shan Ng, M., Luo, J., Chen, B. H., Engelhard, M., Zhong, C. J., Gold–Copper Nanoparticles: Nanostructural Evolution and Bifunctional Catalytic Sites, *Chem. Mater.,* **24,** 4662, (2012).

203. Corthey, G., Giovanetti, L. J., Ramallo-López, J. ü. M., Zelaya, E., Rubert, A. A., Benitez, G. A., Requejo, F. G., Fonticelli, M. H., Salvarezza, R. C., Synthesis and Characterization of Gold@Gold(I)−Thiomalate Core@Shell Nanoparticles, *ACS Nano,* **4,** 3413, (2010).

204. Senoy T, Nair SK, Jamal EMA, S H Al-Harthi, Varma MR, Anantharaman R. Size-dependent surface plasmon resonance in silver silica nanocomposites. Nanotechnology 19[7], 075710. 2008.

205. Yu, D., Yam, V. W.-W., Hydrothermal-Induced Assembly of Colloidal Silver Spheres into Various Nanoparticles on the Basis of HTAB-Modified Silver Mirror Reaction, *J. Phys. Chem. B,* **109,** 5497, (2005).

206. Yuhas, B. D., Habas, S. E., Fakra, S. C., Mokari, T., Probing Compositional Variation within Hybrid Nanostructures, *ACS Nano,* **3,** 3369, (2009).

207. Christensen, S. T., Feng, H., Libera, J. L., Guo, N., Miller, J. T., Stair, P. C., Elam, J. W., Supported Ru–Pt Bimetallic Nanoparticle Catalysts Prepared by Atomic Layer Deposition, *Nano Lett.,* **10,** 3047, (2010).

208. Hong, J. I., Choi, J., Jang, S. S., Gu, J., Chang, Y., Wortman, G., Snyder, R. L., Wang, Z. L., Magnetism in Dopant-Free ZnO Nanoplates, *Nano Lett.,* **12,** 576, (2012).

209. Moreau, L. M., Ha, D. H., Bealing, C. R., Zhang, H., Hennig, R. G., Robinson, R. D., Unintended Phosphorus Doping of Nickel Nanoparticles during Synthesis with TOP: A Discovery through Structural Analysis, *Nano Letters,* **12,** 4530, (2012).

210. Lee, J. R. I., Whitley, H. D., Meulenberg, R. W., Wolcott, A., Zhang, J. Z., Prendergast, D., Lovingood, D. D., Strouse, G. F., Ogitsu, T., Schwegler, E., Terminello, L. J., van Buuren, T., Ligand-Mediated Modification of the Electronic Structure of CdSe Quantum Dots, *Nano Lett.,* **12,** 2763, (2012).

211. Ade, H., Stoll, H., Near-edge X-ray absorption fine-structure microscopy of organic and magnetic materials, *Nat. Mater.,* **8,** 281, (2009).

212. Rodríguez, A. F., Kleibert, A., Bransmann, J., NBolting, F., Probing single magnetic nanoparticles by polarization-dependent soft x-ray absorption spectromicroscopy, *J. Phys. D: Appl. Phys.,* **43,** 474006, (2010).

213. Midgley, P. A., Dunin-Borkowski, R. E., Electron tomography and holography in materials science, *Nat. Mater.,* **8,** 271, (2009).

214. Wang, C., Baer, D. R., Amonette, J. E., Engelhard, M. H., Antony, J., Qiang, Y., Morphology and Electronic Structure of the Oxide Shell on the Surface of Iron Nanoparticles, *J. Am. Chem. Soc.,* **131,** 8824, (2009).

215. Rossouw, D., Botton, G. A., Najafi, E., Lee, V., Hitchcock, A. P., Metallic and Semiconducting Single-Walled Carbon Nanotubes: Differentiating Individual SWCNTs by Their Carbon 1s Spectra, *ACS Nano,* **6,** 10965, (2012).

216. Khursheed A, Luo T. Transmission EELS attachment for SEM. Physical and Failure Analysis of Integrated Circuits, 2005.IPFA 2005.Proceedings of the 12th International Symposium on the. Physical and Failure Analysis of Integrated Circuits, 2005.IPFA 2005.Proceedings of the 12th International Symposium on the , 298-301. 2005.

217. Mirsaleh-Kohan, N., Iberi, V., Simmons, P. D., Bigelow, N. W., Vaschillo, A., Rowland, M. M., Best, M. D., Pennycook, S. J., Masiello, D. J., Guiton, B. S., Camden, J. P., Single-Molecule Surface-Enhanced Raman Scattering: Can STEM/EELS Image Electromagnetic Hot Spots?, *J. Phys. Chem. Lett.,* **3,** 2303, (2012).

218. Utsunomiya, S., Ewing, R. C., Application of High-Angle Annular Dark Field Scanning Transmission Electron Microscopy, Scanning Transmission Electron Microscopy-Energy Dispersive X-ray Spectrometry, and Energy-Filtered Transmission Electron Microscopy to the Characterization of Nanoparticles in the Environment, *Environ. Sci. Technol.,* **37,** 786, (2003).

219. Wang, G., Gao, Z., Tang, S., Chen, C., Duan, F., Zhao, S., Lin, S., Feng, Y., Zhou, L., Qin, Y., Microwave Absorption Properties of Carbon Nanocoils Coated with Highly Controlled Magnetic Materials by Atomic Layer Deposition, *ACS Nano,* **6,** 11009, (2012).

220. Gilbert, B., Fakra, S. C., Xia, T., Pokhrel, S., Mädler, L., Nel, A. E., The Fate of ZnO Nanoparticles Administered to Human Bronchial Epithelial Cells, *ACS Nano,* **6,** 4921, (2012).

221. Nurmi, J. T., Tratnyek, P. G., Sarathy, V., Baer, D. R., Amonette, J. E., Pecher, K., Wang, C., Linehan, J. C., Matson, D. W., Penn, R. L., Driessen, M. D., Characterization and Properties of Metallic Iron Nanoparticles:Spectroscopy, Electrochemistry, and Kinetics, *Environ. Sci. Technol.,* **39,** 1221, (2004).

222. Felten, A., Bittencourt, C., Pireaux, J. J., Reichelt, M., Mayer, J., Hernandez-Cruz, D., Hitchcock, A. P., Individual Multiwall Carbon Nanotubes Spectroscopy by Scanning Transmission X-ray Microscopy, *Nano Lett.,* **7,** 2435, (2007).

223. Panagiotopoulos, N. T., Diamanti, E. K., Koutsokeras, L. E., Baikousi, M., Kordatos, E., Matikas, T. E., Gournis, D., Patsalas, P., Nanocomposite Catalysts Producing Durable, Super-Black Carbon Nanotube Systems: Applications in Solar Thermal Harvesting, *ACS Nano,* **6,** 10475, (2012).

224. Coronado, E., Forment-Aliaga, A., Pinilla-Cienfuegos, E., Tatay, S., Catala, L., Plaza, J. A., Nanopatterning of Anionic Nanoparticles based on Magnetic Prussian-Blue Analogues, *Adv. Funct. Mater.,* **22,** 3625, (2012).

225. Liu, J., Hembree, G. G., Spinnler, G. E., Venables, J. A., High resolution Auger electron spectroscopy and microscopy of a supported metal catalyst, *Surf. Sci.,* **262,** L111-L117, (1992).

226. Cho, S. J., Shahin, A. M., Long, G. J., Davies, J. E., Liu, K., Grandjean, F., Kauzlarich, S. M., Magnetic and Mössbauer Spectral Study of Core/Shell Structured Fe/Au Nanoparticles, *Chem. Mater.,* **18,** 960, (2006).

227. Yathindranath, V., Rebbouh, L., Moore, D. F., Miller, D. W., van Lierop, J., Hegmann, T., A Versatile Method for the Reductive, One-Pot Synthesis of Bare, Hydrophilic and Hydrophobic Magnetite Nanoparticles, *Adv. Funct. Mater.,* **21,** 1457, (2011).

228. Sugimoto, Y., Pou, P., Abe, M., Jelinek, P., Perez, R., Morita, S., Custance, O., Chemical identification of individual surface atoms by atomic force microscopy, *Nature,* **446,** 64, (2007).

229. Shluger, A., Trevethan, T., Microscopy: Atomic fingerprinting, *Nature,* **446,** 34, (2007).

230. Noy, A., Frisbie, C. D., Rozsnyai, L. F., Wrighton, M. S., Lieber, C. M., Chemical Force Microscopy: Exploiting Chemically-Modified Tips To Quantify Adhesion, Friction, and Functional Group Distributions in Molecular Assemblies, *J. Amer. Chem. Soc.,* **117,** 7943, (1995).

231. Schiffres, S. N., Kim, K. H., Hu, L., McGaughey, A. J. H., Islam, M. F., Malen, J. A., Gas Diffusion, Energy Transport, and Thermal Accommodation in Single-Walled Carbon Nanotube Aerogels, *Adv. Funct. Mater.,* **22,** 5251, (2012).

232. Maurer-Jones, M. A., Lin, Y. S., Haynes, C. L., Functional Assessment of Metal Oxide Nanoparticle Toxicity in Immune Cells, *ACS Nano,* **4,** 3363, (2010).

233. George, S., Pokhrel, S., Xia, T., Gilbert, B., Ji, Z., Schowalter, M., Rosenauer, A., Damoiseaux, R., Bradley, K. A., Ma¦êdler, L., Nel, A. ü. E., Use of a Rapid Cytotoxicity Screening Approach To Engineer a Safer Zinc Oxide Nanoparticle through Iron Doping, *ACS Nano,* **4,** 15, (2009).

234. Diwakar, P. K., Loper, K. H., Matiaske, A. M., Hahn, D., Laser-induced breakdown spectroscopy for analysis of micro and nanoparticles, *J. Anal. At. Spectrom.,* (2012).

235. Bundschuh, T., Wagner, T. U., K+Âster, R., Laser-induced Breakdown Detection (LIBD) for the Highly Sensitive Quantification of Aquatic Colloids. Part I: Principle of LIBD and Mathematical Model, *Part. Part. Syst. Charact.,* **22,** 172, (2005).

236. Bundschuh, T., Wagner, T. U., Köster, R., Laser-induced Breakdown Detection (LIBD) for the Highly Sensitive Quantification of Aquatic Colloids. Part II: Experimental Setup of LIBD and Applications, *Part. Part. Syst. Charact.,* **22,** 181, (2005).

237. Bundschuh, T., Knopp, R., Kim, J. I., Laser-induced breakdown detection (LIBD) of aquatic colloids with different laser systems, *Colloids Surf. , A,* **177,** 47, (2001).

238. Choi, S. J., Yoh, J. J., Effective laser-induced breakdown spectroscopy (LIBS) detection using double pulse at optimum configuration., *Appl Spectrosc,* **65,** 952, (2011).

239. Lapresta-Fernández, A., Fernández, A., Blasco, J., Nanoecotoxicity effects of engineered silver and gold nanoparticles in aquatic organisms, *TrAC, Trends Anal. Chem.,* **32,** 40, (2012).

240. Sahu, A., Kang, M. S., Kompch, A., Notthoff, C., Wills, A. W., Deng, D., Winterer, M., Frisbie, C. D., Norris, D. J., Electronic Impurity Doping in CdSe Nanocrystals, *Nano Lett.,* **12,** 2587, (2012).

241. Voinov, M. A., Pagán, J. O. S., Morrison, E., Smirnova, T. I., Smirnov, A. I., Surface-Mediated Production of Hydroxyl Radicals as a Mechanism of Iron Oxide Nanoparticle Biotoxicity, *J. Am. Chem. Soc.,* **133,** 35, (2011).

242. Haiss, W., Thanh, N. T. K., Aveyard, J., Fernig, D. G., Determination of Size and Concentration of Gold Nanoparticles from UV−Vis Spectra, *Anal. Chem.,* **79,** 4215, (2007).

243. Mulvaney, P., Surface Plasmon Spectroscopy of Nanosized Metal Particles, *Langmuir,* **12,** 788, (1996).

244. Thomas, K. G., Barazzouk, S., Ipe, B. I., Joseph, S. T. S., Kamat, P. V., Uniaxial Plasmon Coupling through Longitudinal Self-Assembly of Gold Nanorods, *J. Phys. Chem. B,* **108,** 13066, (2004).

245. Diegoli, S., Manciulea, A. L., Begum, S., Jones, I. P., Lead, J. R., Preece, J. A., Interaction between manufactured gold nanoparticles and naturally occurring organic macromolecules, *Sci. Total Environ.,* **402,** 51, (2008).

246. Neely, A., Perry, C., Varisli, B., Singh, A. K., Arbneshi, T., Senapati, D., Kalluri, J. R., Ray, P. C., Ultrasensitive and Highly Selective Detection of Alzheimers Disease Biomarker Using Two-Photon Rayleigh Scattering Properties of Gold Nanoparticle, *ACS Nano,* **3,** 2834, (2009).

247. McFarland, A. D., Van Duyne, R. P., Single Silver Nanoparticles as Real-Time Optical Sensors with Zeptomole Sensitivity, *Nano Lett.,* **3,** 1057, (2003).

248. Skrabalak, S. E., Chen, J., Sun, Y., Lu, X., Au, L., Cobley, C. M., Xia, Y., Gold Nanocages: Synthesis, Properties, and Applications, *Acc. Chem. Res.,* **41,** 1587, (2008).

249. Cobley, C. M., Xia, Y., Engineering the properties of metal nanostructures via galvanic replacement reactions, *Mater. Sci. Eng. , R,* **70,** 44, (2010).

250. Khan, A., Preparation and characterization of magnetic nanoparticles embedded in microgels, *Mater. Lett.,* **62,** 898, (2007).

251. Tie, S. L., Lee, H. C., Bae, Y. S., Kim, M. B., Lee, K., Lee, C. H., Monodisperse Fe3O4/Fe@SiO2 core/shell nanoparticles with enhanced magnetic property, *Colloids Surf. , A,* **293,** 278, (2007).

252. Lok, C. N., Ho, C. M., Chen, R., He, Q. Y., Yu, W. Y., Sun, H., Tam, P., Chiu, J. F., Che, C. M., Silver nanoparticles: partial oxidation and antibacterial activities, *J. Biol. Inorg. Chem.,* **12,** 527, (2007).

253. Matschulat, A., Drescher, D., Kneipp, J., Surface-Enhanced Raman Scattering Hybrid Nanoprobe Multiplexing and Imaging in Biological Systems, *ACS Nano,* **4,** 3259, (2010).

254. Zhang, D., Neumann, O., Wang, H., Yuwono, V. M., Barhoumi, A., Perham, M., Hartgerink, J. D., Wittung-Stafshede, P., Halas, N. J., Gold Nanoparticles Can Induce the Formation of Protein-based Aggregates at Physiological pH, *Nano Lett.,* **9,** 666, (2009).

255. Ansar, S. M., Haputhanthri, R., Edmonds, B., Liu, D., Yu, L., Sygula, A., Zhang, D., Determination of the Binding Affinity, Packing, and Conformation of Thiolate and Thione Ligands on Gold Nanoparticles, *J. Phys. Chem. C,* **115,** 653, (2011).

256. Contreras-Cáceres, R., Pastoriza-Santos, I., Álvarez-Puebla, R., Pérez-Juste, J., Fernández-Barbero, A., Liz-Marzán, L. M., Growing Au/Ag Nanoparticles within

Microgel Colloids for Improved Surface-Enhanced Raman Scattering Detection, *Chem. Eur. J.,* **16,** 9462, (2010).

257. Perez-Juste, J., Pastoriza-Santos, I., Liz-Marzan, L. M., Multifunctionality in metal@microgel colloidal nanocomposites, *J. Mater. Chem. A,* **1,** 20, (2013).

258. Jin, R., Qian, H., Wu, Z., Zhu, Y., Zhu, M., Mohanty, A., Garg, N., Size Focusing: A Methodology for Synthesizing Atomically Precise Gold Nanoclusters, *J. Phys. Chem. Lett.,* **1,** 2903, (2010).

259. Fields-Zinna, C. A., Parker, J. F., Murray, R. W., Mass Spectrometry of Ligand Exchange Chelation of the Nanoparticle [Au25(SCH2CH2C6H5)18]1 by CH3C6H3(SH)2, *J. Am. Chem. Soc.,* **132,** 17193, (2010).

260. Navin, J. K., Grass, M. E., Somorjai, G. A., Marsh, A. L., Characterization of Colloidal Platinum Nanoparticles by MALDI-TOF Mass Spectrometry, *Anal. Chem.,* **81,** 6295, (2009).

261. Dass, A., Stevenson, A., Dubay, G. R., Tracy, J. B., Murray, R. W., Nanoparticle MALDI-TOF Mass Spectrometry without Fragmentation: Au25(SCH2CH2Ph)18 and Mixed Monolayer Au25(SCH2CH2Ph)18-x(L)(x), *J. Am. Chem. Soc.,* **130,** 5940, (2008).

262. Peng, W.-P., Cai, Y., Lee, Y. T., Chang, H.-C., Laser-induced fluorescence/ion trap as a detector for mass spectrometric analysis of nanoparticles, *Int J Mass Spectrom,* **229,** 67, (2003).

263. Snively, C. M., Lauterbach, J., Sampling accessories for the high-throughput analysis of combinatorial libraries using spectral imaging, *Spectroscopy,* **17,** 26, (2002).

264. Ammann, A. A., Inductively coupled plasma mass spectrometry (ICP MS): a versatile tool, *J. Mass Spectrom.,* **42,** 419, (2007).

265. Montoro Bustos, A. R., Encinar, J. R., Fernandez-Arguelles, M. T., Costa-Fernandez, J. M., Sanz-Medel, A., Elemental mass spectrometry: a powerful tool for an accurate characterisation at elemental level of quantum dots, *Chem. Commun.,* **0,** 3107, (2009).

266. Trapiella-Alfonso, L., Montoro Bustos, A. R., Encinar, J. R., Costa-Fernandez, J. M., Pereiro, R., Sanz-Medel, A., New integrated elemental and molecular strategies as a diagnostic tool for the quality of water soluble quantum dots and their bioconjugates, *Nanoscale,* **3,** 954, (2011).

267. Shiundu, P. M., Munguti, S. M., Ratanathanawongs Williams, S. K., Retention behavior of metal particle dispersions in aqueous and nonaqueous carriers in thermal field-flow fractionation, *J. Chromatogr. , A,* **983,** 163, (2003).

268. Al-Ammar, A., Siripinyanond, A., Barnes, M., Simultaneous sample preconcentration and matrix removal using field-flow fractionation coupled to inductively coupled plasma mass spectrometry, *Spectrochim. Acta, Part B,* **56,** 1951, (2001).

269. Jackson, B. P., Ranville, J. F., Bertsch, P. M., Sowder, A. G., Characterization of Colloidal and Humic-Bound Ni and U in the Dissolved Fraction of Contaminated Sediment Extracts, *Environ. Sci. Technol.,* **39,** 2478, (2005).

270. Hassellöv, M., Lyvén, B., Haraldsson, C., Sirinawin, W., Determination of Continuous Size and Trace Element Distribution of Colloidal Material in Natural Water by On-Line Coupling of Flow Field-Flow Fractionation with ICPMS, *Anal. Chem.,* **71,** 3497, (1999).

271. Baalousha, M., Kammer, V. D., Motelica-Heino, M., Baborowski, M., Hofmeister, C., Le Coustumer, P., Size-Based Speciation of Natural Colloidal Particles by Flow Field Flow Fractionation, Inductively Coupled Plasma-Mass Spectroscopy, and Transmission Electron Microscopy/X-ray Energy Dispersive Spectroscopy:ΓÇë ColloidsΓêÆTrace Element Interaction, *Environ. Sci. Technol.,* **40,** 2156, (2006).

272. Trefry, J. C., Monahan, J. L., Weaver, K. M., Meyerhoefer, A. J., Markopolous, M. M., Arnold, Z. S., Wooley, D. P., Pavel, I. E., Size Selection and Concentration of Silver Nanoparticles by Tangential Flow Ultrafiltration for SERS-Based Biosensors, *J. Am. Chem. Soc.,* **132,** 10970, (2010).

273. Lapresta-Fernández, A., Fernández, A., Blasco, J., Public concern over ecotoxicology risks from nanomaterials: Pressing need for research-based information, *Environment International,* **39,** 148, (2012).

274. European Commission, Scientific Committee on Emerging and Newly-Identified Health Risks (SCENIHR). The appropriateness of the risk assessment methodology in accordance with the Technical Guidance Documents for new and existing substances for assessing the risks of nanomaterials. Part Fibre Toxicol 21–22 June 2007. 2007. Brussels, Belgium., European Commission.

275. Silva, B. F. d., Pérez, S., Gardinalli, P., Singhal, R. K., Mozeto, A. A., Barceló, D., Analytical chemistry of metallic nanoparticles in natural environments, *TrAC, Trends Anal. Chem.,* **30,** 528, (2011).

276. Nan, F., Song, C., Zhang, J., Hui, R., Chen, J., Fairbridge, C., Botton, G. A., STEM HAADF Tomography of Molybdenum Disulfide with Mesoporous Structure, *ChemCatChem,* **3,** 999, (2011).

277. Yin Win, K., Feng, S. S., Effects of particle size and surface coating on cellular uptake of polymeric nanoparticles for oral delivery of anticancer drugs, *Biomaterials,* **26,** 2713, (2005).

278. Lapresta-Fernández, A., Cywinski, P., Moro, A., Mohr, G., Fluorescent polyacrylamide nanoparticles for naproxen recognition, *Anal. Bioanal. Chem.,* **395,** 1821, (2009).

279. Chen, H., Kou, X., Yang, Z., Ni, W., Wang, J., Shape- and Size-Dependent Refractive Index Sensitivity of Gold Nanoparticles, *Langmuir,* **24,** 5233, (2008).

280. Corr, S. A., Rakovich, Y. P., Gun'ko, Y. K., Multifunctional Magnetic-fluorescent Nanocomposites for Biomedical Applications, *Nanoscale Res Lett,* **3,** 87, (2008).

281. Cobley, C. M., Xia, Y., Engineering the properties of metal nanostructures via galvanic replacement reactions, *Mater. Sci. Eng. , R,* **70,** 44, (2010).